

AN ABSTRACT OF THE THESIS OF

Jordan J. Danielson for the degree of Master of Science in Nuclear Engineering
presented on November 18, 2016.

Title: Gravity-Based Non-Invasive Superconducting Gravimeter System for
Reactor Coolant Inventory Monitoring

Abstract approved: _____

Qiao Wu

All nuclear reactors rely heavily on the use of level sensing instrumentation to detect the behaviour of liquid in vessels. The majority of level sensing instruments are differential pressure sensing meters, which are invasive and could be the failure source in the pressure boundary of the primary coolant system. In this thesis, a new method for detecting the coolant inventory in nuclear reactors using superconducting gravimeters is investigated experimentally. A differential volume simulation from Information Systems Laboratories, Inc. is modified and used to predict the gravitational acceleration seen by the superconducting gravimeters. This model is then evaluated by comparing simulations to data taken at a scaled model of the NuScale, Inc. small modular reactor. The data is obtained using two iGravTM superconducting gravimeters from GWR, Inc. to measure water inventory in the NIST-1 facility at Oregon State University. Overall, the simulation can reasonably predict the signal that will be seen by the gravimeters, but requires further investigation in to tidal simulation in order for the gravimeters to be a reliable instrument in nuclear facilities.

©Copyright by Jordan J. Danielson
November 18, 2016
All Rights Reserved

Gravity-Based Non-Invasive Superconducting Gravimeter System for
Reactor Coolant Inventory Monitoring

by

Jordan J. Danielson

A THESIS

submitted to

Oregon State University

in partial fulfillment of
the requirements for the
degree of

Master of Science

Presented November 18, 2016
Commencement June 2017

Master of Science thesis of Jordan J. Danielson presented on November 18, 2016.

APPROVED:

Major Professor, representing Nuclear Engineering

Head of the School of Nuclear Science and Engineering

Dean of the Graduate School

I understand that my thesis will become part of the permanent collection of Oregon State University libraries. My signature below authorizes release of my thesis to any reader upon request.

Jordan J. Danielson, Author

ACKNOWLEDGEMENTS

I would first like to thank my wife, Kate, for supporting and encouraging me through the years it took to complete this process. I wouldn't have been able to do it without you. Thanks to my family for constantly believing in me and setting the bar high in all walks of life.

I would also like to thank Dr. Wu for allowing me to have this great opportunity, and for all the lessons and guidance he has given me. I would like to thank both Richard Warburton and Richard Reineman of GWR, Inc. not only for providing the gravimeters to make this study possible, but for their integral role in producing data and supporting this project. A final thank you goes to Jeff Ridgway at ISL, Inc. for your guidance, patience, and understanding throughout this process.

TABLE OF CONTENTS

	<u>Page</u>
1 Introduction	1
1.1 Background	1
1.1.1 Domestic History of Nuclear Designs	1
1.1.2 Small Modular Reactors	3
1.1.3 NuScale Power, Inc.	4
1.1.4 Current Liquid Level Measurement	9
1.2 Objectives	10
1.3 Document Overview	11
2 Literature Review	12
2.1 Standard Liquid Level Measurement in Reactors	12
2.1.1 Uncertainty for Non-Pressurized Vessel	15
2.1.2 Uncertainty for Pressurized Vessel	18
2.2 Gravimeters	19
2.2.1 iGrav TM Superconducting Gravimeter System	24
2.2.2 Superconducting Gravimeter Measurements	29
2.2.3 iGrav TM Uncertainty Estimation	31
3 Methods	35
3.1 Simulation	35
3.2 Experiment	43
3.2.1 NIST-1 Facility Description	43
3.2.2 Current Level Measurement	48
3.2.3 iGrav System Configuration	49
3.2.4 Signal Creation Procedure	52
4 Results & Discussion	54
4.1 Simulation	54
4.2 CPV Characterization Experiment	56
4.3 Raw Data	56
4.4 Tide Removal	59
4.5 Comparison	61
4.5.1 G03 Gravimeter	62

TABLE OF CONTENTS (Continued)

	<u>Page</u>
4.5.2 G13 Gravimeter	71
4.6 Signal Subtraction	77
4.7 Discussion	81
5 Conclusion	83
5.1 Summary	83
5.2 Future Work	84
Bibliography	86

LIST OF FIGURES

Figure	Page
1.1 Cross-sectional View of NuScale SMR Prototype Design, [1]	5
1.2 Example of a Single-Phase Natural Circulation Reactor, [2]	7
2.1 Rosemount Differential Pressure Transmitter model 3051S, [3]	13
2.2 SG Sphere, Capacitive Plates, and Coil Configuration [4]	22
2.3 The iGrav TM Superconducting Gravimeter System from GWR, courtesy of Dr. Richard Warburton of GWR [5]	25
2.4 Cross-section of the iGrav TM Dewar, [6]	26
2.5 An Example of the Impact of a Linear Instrumental Drift, [7]	30
2.6 PSD $((nm/s^2)^2/Hz)$ vs. Signal Frequency (Hz) for Various Gravimeters [8]	32
3.1 Simulation Sensitivity to Changing Number of Points Along Z-Axis	39
3.2 Difference in Simulation Signal with Changing Number of Points Along Z-Axis	39
3.3 Simulation Sensitivity to Changing Number of Points Along R-Axis	40
3.4 Simulation Sensitivity to Changing Number of Points Along R-Axis	41
3.5 Simulation Sensitivity to Changing Number of Points Along θ -Axis	42
3.6 Simulation Sensitivity to Changing Number of Points Along θ -Axis	42
3.7 Overhead View of NIST-1 Facility, I made	44
3.8 Configuration of LDP-6001 during Experiment	49
3.9 iGrav 03 and 13 Location Dimensions	51
4.1 CPV Water Level Throughout Entire Experiment	56
4.2 G03 Gravimeter Raw Signal Throughout Entire Experiment	57
4.3 G13 Gravimeter Raw Signal Throughout Entire Experiment	58

LIST OF FIGURES (Continued)

<u>Figure</u>	<u>Page</u>
4.4 G03 Data with Tides Subtracted, and Simulation Throughout Experiment	59
4.5 G13 Data with Tides Subtracted, and Simulation Throughout Experiment	60
4.6 Event 1 CPV Level from LDP-6001	63
4.7 Event 1 G03 Gravimeter Signal and Simulation	63
4.8 Event 2 CPV Level from LDP-6001	64
4.9 Event 2 G03 Gravimeter Signal and Simulation	64
4.10 Event 3 CPV Level from LDP-6001	65
4.11 Event 3 G03 Gravimeter Signal and Simulation	65
4.12 Event 4 CPV Level from LDP-6001	66
4.13 Event 4 G03 Gravimeter Signal and Simulation	66
4.14 Event 5 CPV Level from LDP-6001	67
4.15 Event 5 G03 Gravimeter Signal and Simulation	67
4.16 Event 6 CPV Level from LDP-6001	68
4.17 Event 6 G03 Gravimeter Signal and Simulation	68
4.18 Event 1 G13 Gravimeter Signal and Simulation	72
4.19 Event 2 G13 Gravimeter Signal and Simulation	72
4.20 Event 3 G13 Gravimeter Signal and Simulation	73
4.21 Event 4 G13 Gravimeter Signal and Simulation	73
4.22 Event 5 G13 Gravimeter Signal and Simulation	74
4.23 Event 6 G13 Gravimeter Signal and Simulation	74
4.24 Event 1 Subtraction Signal and Simulation	77
4.25 Event 2 Subtraction Signal and Simulation	78

LIST OF FIGURES (Continued)

<u>Figure</u>	<u>Page</u>
4.26 Event 3 Subtraction Signal and Simulation	78
4.27 Event 4 Subtraction Signal and Simulation	79
4.28 Event 5 Subtraction Signal and Simulation	79
4.29 Event 6 Subtraction Signal and Simulation	80

LIST OF TABLES

<u>Table</u>		<u>Page</u>
3.1	Gravimeter Locations	51
4.1	Simulation of NIST-1 Vessel Signals	55
4.2	Zero RMS Signals for G03	62
4.3	G03 Results for Entire Experiment	69
4.4	Zero RMS Signals for G13	71
4.5	G13 Results for Entire Experiment	75

Chapter 1: Introduction

This thesis examines the feasibility of utilizing specialized instruments called gravimeters, to directly and non-invasively measure liquid mass in a vessel. In this introduction, a brief history of the design used throughout the nuclear power industry is presented, followed by a description of the specific design that would most likely benefit from this research. Current methods for measuring liquid inventory and associated drawbacks are introduced, the objectives for this study are defined, and a document overview is provided.

1.1 Background

1.1.1 Domestic History of Nuclear Designs

Nuclear energy has been a staple of the United States energy production since the foundation of the Atomic Energy Commission with the passing of the Atomic Energy Act of 1946. This historic piece of legislation laid the foundation for how the United States would allow nuclear power development under civilian control, starting a somewhat rocky but brilliant path to utilizing fission in electricity generation. The partnership between the United States government and civilian research has led to many important advancements in the nuclear industry. Through the 1950s to 1970s, nuclear energy flourished as developments in the industry came to market, and additional pieces of helpful legislation were passed by the government. The first design used to create electricity, the Experimental Breeder Reactor (EBR-1), came out of Argonne National Lab in 1951 [9]. Even though it was not specifically designed to do so, the core of EBR-1, while not being much larger than a football,

generated enough electricity to light four 200 Watt light bulbs. After a few design improvements, EBR-1 was able to produce approximately 200 kW of electricity (200kW_e). While this might not seem like much, the nuclear industry quickly took advantage of the principal of economy of scale, and within 10 years, Westinghouse designed and started the operation of the 250 MW_e pressurized water reactor (PWR) Yankee Rowe, in Rowe, Massachusetts. With continuing advances in technology, at the end of the 1960s PWRs and General Electronic's boiling water reactor (BWR) were capable of generating 1000 MW_e . These reactors require immense structures to house the large vessels used to contain the various components of the nuclear power generation cycle. Many of these reactors continue to produce electricity, but are requiring extensions to their operating licenses or face being decommissioned [10], as the commercial nuclear power generation industry stagnated between the mid 1970s and mid 2000s. In February of 2010, the President of the United States, Barack Obama, expanded the Energy Policy Act of 2005 to triple the already authorized \$18.5 billion in order to expand commercial nuclear power. This directly led to the most recent nuclear reactors being constructed in Vogtle, Georgia. This design transition throughout the history of nuclear reactors is organized into four sections, or generations. The group of generation I reactors consists of experimental reactors, like EBR-1. The first generation of reactors paved the way for the modern designs by testing and refining what were new and radical breakthroughs in nuclear science. Almost all commercial reactors in operation today are considered generation II reactors. The aforementioned Yankee Rowe reactor is considered to be among the first wave of generation II designs. These reactors are specialized to produce large amounts of baseline electricity for a longer time. Baseline electricity refers to the minimum amount of electricity that must be generated on a day-by-day basis. These reactors are meant to continually produce maximum output, except during maintenance and refueling outages. They are much larger than the generation I reactors, and utilize active safety features, which require human intervention or electrical power to operate. The next generation of reactors to just recently hit the market are generation III designs.

The designs in this category incorporate passive safety systems, allowing them to operate without human intervention and onsite/offsite electrical power during an accident. The two newest units under construction in Vogtle, both AP1000 PWRs designed by Westinghouse, are a testament to the advancement the industry has fostered in light of some of the severe accidents in nuclear energy generation's history. Though the new plants will be the state of the art in every way possible for large scale PWRs, new research in the nuclear industry focuses on the idea of scalable, and/or modular, infrastructure [11] like Small Modular Reactors (SMR). With the support of the U.S. Department of Energy, the research performed in this thesis will support the continual effort to make the nuclear electrical generation industry as safe as possible.

1.1.2 Small Modular Reactors

In the nuclear power industry, technological innovation mainly aims to make the reactors as safe as possible in both normal operating conditions and in the rare case of an accident. Many lessons have been learned from the recent accident at the Fukushima-Daiichi nuclear power plant in Japan, and innovations emerge for better reactor safety performance. One example is through the development of SMRs. A nuclear reactor is considered to be "small" if the design output is 300 MW_e or less [11]. In comparison, some of the nuclear reactors currently under construction have a design output of 1000 MW_e or greater. Smaller power outputs allow for greater control over the reactor, and meet the energy needs with a scalable approach, making nuclear energy a viable source of baseline electricity for smaller communities and remote areas. The modularity of a reactor refers to the ability of the major components, such as the pressure vessel(s), to be manufactured in a central location, and then sent to the building site. This is advantageous in the nuclear industry because it allows quicker and cheaper repair of larger components in a well regulated environment and condition. It can significantly reduce down time required for maintenance, allow for shorter construction times, and even in-

crease the lifetime of the plant (for example the San Onofre nuclear power plant was shut down prematurely due to a required fix to the steam generator which would not have been economically feasible). Another innovative design concept being introduced to the current reactors includes passive safety systems. A passive safety system is one which requires neither electricity to function, nor human intervention to react to accident scenarios. An example of a passive safety system would be one where pressure relief valves automatically fail in a safe condition to allow pressure to be controlled in a safe manner during an accident scenario. All of these design features, and more, are included in what is considered generation III and generation III+ reactor designs.

1.1.3 NuScale Power, Inc.

The NuScale nuclear reactor, designed by NuScale Power Inc., is a generation III+ pressurized, light water reactor (LWR), that leverages natural circulation to drive coolant flow through the primary system. The design integrates all the primary loop components in a Reactor Pressure Vessel (RPV), including a core, which is located at the bottom of the RPV, a pressurizer at the top that connects to the primary coolant through a baffle plate with a narrow opening, a secondary system which uses a helical coil steam generator inside the primary coolant flow loop, a containment vessel that encloses the RPV, sitting in a cooling pool that acts as the heat sink during postulated accident transients. Figure 1.1 shows a cross-section of a NuScale SMR in the cooling pool environment. A single "module" is considered to be the RPV and containment system, and in an industrial setting, a single power plant would be able to scale the number of modules up or down depending on the energy needs. Currently, a full sized power plant would consist of 12 modules, each producing approximately 45 MW_e for a total electrical output of around 540 MW_e [12].

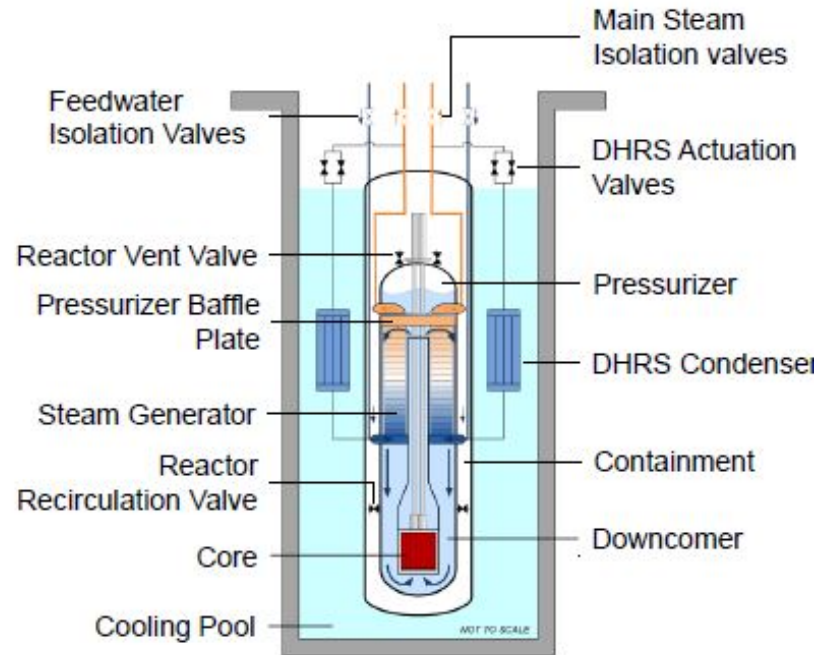


Figure 1.1: Cross-sectional View of NuScale SMR Prototype Design, [1]

A natural circulation loop is used in each of the modules as the method of transporting energy from the core to the helical coil steam generator located in the RPV. This means that the primary system coolant flow is driven by the change in coolant density due to temperature variation in the primary loop from the core, through the steam generator, and back to the core again. Starting from the core, the heated coolant flows up through a riser, then is turned around 180 degrees by a baffle plate, and flows downward in the outer annular portion of the RPV. The heated coolant then passes against a helical coil steam generator, transfers heat to the cooler water flowing inside the coiled tubes, and eventually returns to the core inlet. In the secondary flow loop, the water flow in the helical coil steam generator is provided by a pump and becomes superheated steam at the steam generator exit. This superheated steam then drives a turbine to generate electricity. Surrounding the primary system and the steam generator portion of the secondary system is

the containment vessel (CNV). It is a container held under vacuum that provides a barrier for any accidental coolant leaks or intentional coolant releases to the environment. The RPV is connected to the CNV by several valve configurations, allowing the reactor to be controlled in the event of an accident scenario. Figure 1.1 shows the Reactor Vent Valves, the Reactor Recirculation Valves, and the Decay Heat Removal System. Combined with the natural circulation driving the primary coolant, the requirement of a primary coolant pump is eliminated. This is advantageous because the primary system no longer has to rely on electricity being provided to the pump to drive the flow. This also means that in the case of an accident, the reactor can completely and safely remove the remaining decay heat through the safety systems without requiring electricity. In order to achieve the density difference to drive the flow, a large vertical distance between the heat source (core) and sink (steam generator) is required. This can be seen by performing a closed loop, single-phase momentum balance on the system seen in Figure 1.2. In this figure, the reactor is broken up in to three sections: the cooler lower region (purple), the hotter upper region (red), and the pressurizer section (yellow). Both the red and purple sections make up the primary loop of saturated fluid, where the core (red and black stripes) heats the coolant from a cooler temperature, T_C (purple), to a hotter temperature, T_H (red). The steam generator (horizontal black stripes) cools the coolant from T_H back to T_C , allowing the process to start again. The distance between the core and steam generator is defined as L_{TH} , and the temperature of the superheated steam in the pressurizer section (yellow), is T_{SAT} .

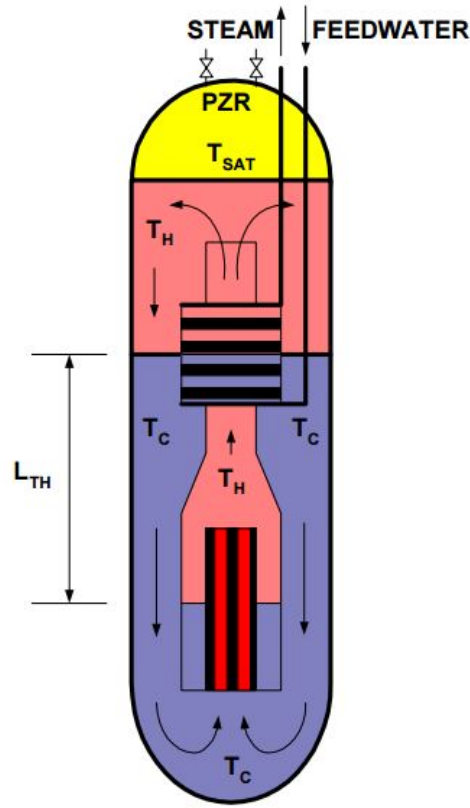


Figure 1.2: Example of a Single-Phase Natural Circulation Reactor, [2]

From the IAEA report on Natural Circulation in Water Cooled Nuclear Power Plants [2], the following conservation of momentum equation is derived:

$$\sum_{i=1}^N \left(\frac{l_i}{a_i} \right) \frac{d\dot{m}}{dt} = \beta g \rho (T_H - T_C) L_{TH} - \frac{\dot{m}^2}{\rho l a_c^2} \sum_{i=1}^N \left[\frac{1}{2} \left(\frac{fl}{d} + K \right)_i \left(\frac{a_c}{a_i} \right)^2 \right] \quad (1.1)$$

The assumptions made to arrive at Equation 1.1, are as follows:

1. One-dimensional flow along the loop axis, making fluid properties uniform at every cross-section
2. The Boussinesq approximation (densities assumed equal except in buoyancy term)
3. Incompressible fluid
4. T_C is constant
5. Form losses are the dominate loss of system

This equation is for a loop of individual components, there is a term summing the effects of the momentum change through each component and the form losses. The first term on the right hand side describes the increase in fluid momentum due to a density difference. This is derived from the gravitational pressure term, where its original form is:

$$\Delta P_g = gL_{TH} (\rho_H - \rho_C) \quad (1.2)$$

Each density term above can be described using the thermal expansion coefficient β multiplied by the temperature. This allows the above equation to equal the first term on the right hand side of equation 1.1. Because of this, the NuScale SMR has a greater vertical height than its lateral width, with a RPV height to inner diameter ratio of about 5.3 [12]. Under accident conditions, monitoring the coolant inventory is of great importance in preventing core melt and structure damage. The tall configuration of the NuScale reactor design allows for the possible use of gravimeters outside the reactor containment to detect the liquid inventory, as the vessels are theorized to not be too wide to have significant loss of signal sensitivity in the horizontal direction. The use of gravimeters to measure level also introduces the possibility that taps would not need to be drilled through the containment and RPV in order to measure liquid level, since the liquid inventory would be measured

directly through its gravitational force on the meter. Eliminating possible points of failure by removing the need for some instrument penetrations would make the pressure boundary stronger and reactors safer.

1.1.4 Current Liquid Level Measurement

Many industrial practices involve the need to measure liquid level in a container to a reasonable degree of certainty, and the nuclear industry is no exception. Throughout the existing designs of nuclear power plants, many different large vessels are required to move the liquid in such a way that the energy from the fission events occurring in the core can be safely transported to produce steam, and that steam can be used to generate electricity to power our modern civilization. Methods for measuring the amount of liquid in these vessels are well established, and are employed throughout all reactor vessel designs.

The most common method currently employed to measure liquid level in reactor vessels involves the use of differential pressure meters. Typically, two holes are drilled through the wall of the vessel to be measured, one at the top most point, and one at the bottom most point. If impulse lines are used, this means that piping from those holes are routed to the differential pressure meter, where the pressure of each line, and therefore the pressure in the vessel at the elevation of the tap, is measured. In more advanced designs, two pressure meters are attached to the holes, and their signals are combined electrically in order to calculate the differential pressure between the holes. The difference in pressure between the two lines can be related directly to the liquid level in the vessel if the density of the liquid is known, meaning that for high temperature/high pressure systems, the level measurement is compensated for these changes from ambient conditions using other instruments in the vessel. There could be disadvantages to using these differential pressure meters, especially concerning the taps and piping from those taps. The taps themselves are possible points of failure, especially when looking at

high pressure systems seen in nuclear reactors. To measure the differential pressure in the NuScale design, the RPV or pressurizer section for instance, the piping leading from the holes must pass through the containment vessel, making more points of possible failure. Even though the lines are small, any rupture occurring within the RPV would require very time consuming maintenance, as the containment would need to be opened in order to access the leak. Another disadvantage of the differential pressure meters is that their measurement relies on the piping from the taps to be completely solid with the liquid to be measured. Any bubbles caught in the line can drastically change the output signal and therefore the liquid level measurement. Because of this, maintenance must be done in order to ensure that there are no bubbles caught in the lines. Although not very likely in reactor systems due to intense filtering of the coolant, the taps can become clogged with debris, which would also give an incorrect liquid level signal.

1.2 Objectives

Measuring the liquid inventory in a vessel is critical to ensuring the safe operation of a nuclear reactor. The primary objective of this work is to assess the feasibility of a non-invasive method of measuring the liquid level in a nuclear reactor. The method under investigation involves the utilization of superconducting gravimeters, specifically the highly sensitive iGravTM system from GWR, Inc. Due to the unique geometry of the NuScale SMR design, it was chosen as the reactor that this method would be applied to. The primary objective was achieved by completing the following secondary objectives:

1. Assess the reliability of a simulation showing expected signal strength seen by a superconducting gravimeter.
2. Use the simulation to model the NIST-1 facility at Oregon State University, a scaled model of the NuScale SMR.

3. Utilize the iGravTM system to map the gravitational signal seen from the NIST-1 facility.
4. Assess the noise seen by the iGravTM system in an industrial environment.
5. Identify optimal sensor locations for further study into the use of the gravimeters in a full scale NuScale SMR.

1.3 Document Overview

This thesis covers the following content:

Chapter 1: Introduction - The nuclear industry and typical instrumentation are introduced, including SMRs. An explanation for the need to further research liquid level detection systems is explained.

Chapter 2: Literature Review - Previous work in the use of gravimeters is established, as well as various techniques currently used to measure liquid level inventory in reactors is explained.

Chapter 3: Methods - The theory behind the simulation is explained in detail. A description of the NIST-1 facility and experimental set-up as well as the procedure performed to obtain the data are explained.

Chapter 4: Results - A presentation of the results of the experiment outlined in the objectives and simulation data.

Chapter 5: Conclusions - Conclusions drawn from the results of the experiment and simulation, as well as possible configurations of a non-invasive coolant inventory monitoring system using gravimeters.

Chapter 2: Literature Review

This section will give a survey of the literature relevant to this thesis. A description of the various methods of measuring liquid inventory in the nuclear industry will be presented. The drawbacks and some current incidents caused by the use of differential pressure meters are outlined. The accuracy of the differential pressure meters used to find liquid level at the NIST-1 facility is characterized. An explanation of the different types of gravimeters and examples of their uses, including the iGravTM system, will be detailed.

2.1 Standard Liquid Level Measurement in Reactors

The most common method of measuring liquid inventory/level in the nuclear industry utilizes differential pressure meters. The meters used on the NIST-1 facility are dual diaphragm differential pressure instruments. Two sensing lines connect the locations where the pressure will be measured on the vessel to the diaphragm in the meter. The diaphragms react to the pressure causing a signal to be created. The signal is a voltage signal, and is related to the pressure across the two lines. Figure 2.1 shows a diaphragm-type differential pressure meter made by Rosemount. The grey section houses the diaphragms, the silver vent valves allow maintenance to ensure the sensing line is filled solidly with liquid, and the blue head houses the electronics and wire connections. Typically, there will also be a manifold which attaches to the bottom of the meter, with manual turn valves to control flow through the sensing lines during maintenance.



Figure 2.1: Rosemount Differential Pressure Transmitter model 3051S, [3]

There are some disadvantages with differential pressure meters, including clogging of the sensing lines, dry/wet sensing line inconsistency, and leakage around the taps and in sensing lines. If the sensing lines are clogged or incompletely filled with fluid (for example having air bubbles in fluid), the signal seen by the meter will be incorrect. This is avoided by using the aforementioned vent valves to allow any blockage between the tap and diaphragm to be carried out of the lines. The United States Nuclear Regulatory Commission (NRC) focuses on how these sensing lines can impact the safety of the reactor in many different reports. Accidents concerning the sensing lines have been encountered in the past, as seen in NRC Regulatory Guide 1.151, [13]. To quote the guide, "Operational events have occurred in which evolved gases in instrument sensing lines have affected measured water levels in operating nuclear power plants." One of the specific instances referred to is outlined in Information Notice No. 95-20 [14]. In this notice, an event

at the St. Lucie site in Florida occurred during routine maintenance involving filling and venting the pressure instruments on the reactor coolant system. A high pressure signal was generated despite the pressure in the reactor coolant system being 50 psig, well below any pressure meant to cause a high pressure signal. Two malfunctioning pressure transmitters exceeded 1712 psig, while two operating pressure transmitters indicated 50 psig. Per design, this pressure difference caused the safety injection system to begin injection. The malfunctioning sensors indicated a high pressure due to the material of the sensing bladder in the transmitters being permeable to monatomic hydrogen. Monatomic hydrogen was created by a reaction between Monel metal and stainless steel. The monatomic hydrogen was trapped in the bladders of the pressure instruments after it had recombined into diatomic hydrogen. The diatomic hydrogen was not able to pass through the bladder. This caused the bladders to swell, giving an erroneous reading.

Another issue concerning pressure instrument sensing lines is the temperature limitation of the sensing bladders. If a sensing bladder is exposed to superheated steam that is beyond the bladders design, the signal from the instrument can be more erratic than normal, and the instrument can be damaged. Another NRC Information Notice [15] was issued when it was found that having non-condensable gasses build up in the condensing pots of the sensing lines of pressure instruments can give unacceptable errors. Condensing pots are attachments to instrument sensing lines that allow any superheated fluid to condense and change state. They are larger than the line, and typically have a venting valve to allow any contents to be drained during maintenance. Condensate pots protect the bladder on the line they are attached, and ensure adequate pressure differences between sensing lines to detect the vessel of interest's conditions. The NRC found that at the Millstone Unit 3 in Waterford, Connecticut, non-condensable gasses had built up in the condensing pots. It was concluded that during a release of non-condensable gases, level indication errors could reach 40% if the issue was not rectified. The uncertainty calculation for the differential pressure meter used to measure the CPV level (LDP-6001) was done in accordance with the NIST-1 quality assurance

program, which adheres to NQA-1 2008 and 2009a, and ASME standards. The iGravTM system uncertainty calculations are done to directly compare the meter's ability with the differential pressure meter.

2.1.1 Uncertainty for Non-Pressurized Vessel

One of the requirements of the NIST-1 quality assurance program is that the uncertainty of the instruments must have a confidence of 95% or greater. All of the following uncertainties, unless calculated or specified, are manufacturer specifications and come a 95% confidence. Therefore, this confidence is carried through with all calculations, unless otherwise specified. The differential pressure meter used in this experiment (LDP-6001), has an instrument range of -1000 to 1000 inches of water. The range over which the instrument was calculated was 0 to 280 inches of water. During calibration, the pressure was measured with Transmation 1090 Pressure Measurement Meter with an uncertainty of 0.02% of the reading. The uncertainty of the 1090 was calculated at the maximum reading of 280 inches of water, giving an uncertainty of 0.056 inches of water. The pressure signal was interpreted using a Transmation Pressure Module SD0412G with an uncertainty of 0.070% of the range from 0 to 33 psig or 0 to 914.3058 inches of water. This gives an uncertainty of 0.6400 inches of water. The uncertainty of the output given by LDP-6001, which is read with a Fluke 45 multimeter, is calculated next. The output of LDP-6001 is in mADC with a range of 4 to 20 mADC. The manufacturer specified uncertainty with the Fluke 45 is 0.050% of the range + 3*LSD, where LSD stands for the "Lowest Significant Digit" and is the smallest digit of resolution on the display of the meter. The Fluke 45 multimeter reads the mADC output from LDP-6001 in the 0 to 30 mADC range. Since the maximum output signal for LDP-6001 is 20 mADC, this is where the uncertainty is applied, so the full range of the calibration is covered. This results in an output uncertainty of $(20 \text{ mADC}) \cdot (0.05\%) + 3 \cdot (0.001 \text{ mADC}) = 0.013 \text{ mADC}$. Since the signal of 20 mADC is associated with the maximum measurement of the calibrated range (20

mADC - 4 mADC = 16 mADC), the uncertainty in mADC can be converted to inches of water using the following equation:

$$U_{inches} = U_{mADC} \left(\frac{280}{16} \right) \quad (2.1)$$

This gives an uncertainty for the Fluke 45 of 0.2275 inches of water. The total calibration uncertainty can be found by calculating the root of the sum of the square of the individual uncertainties, as shown in the following equation:

$$\begin{aligned} U_{cal} &= \sqrt{U_1^2 + U_2^2 + \dots + U_n^2} \\ &= \sqrt{0.056^2 + 0.6400^2 + 0.2275^2} \\ &= 0.6816 \text{ inH}_2\text{O} \end{aligned} \quad (2.2)$$

Where U_1, U_2, \dots, U_n is the individual instrumentation uncertainty, and U_{cal} is the total calibration uncertainty of the signal after going through each calibration instrument. The specification limit (SL) of the instrument can then be calculated using the following formula:

$$SL = TL + \left(U_{cal} \frac{1.64}{2} \right) \quad (2.3)$$

Where TL is the tolerance limit specified by the NIST-1 quality assurance program. The tolerance limit for LDP-6001 is 0.25% of the calibrated span, or 0.70 inches of water. The SL before environmental effects for LDP-6001 is therefore 1.2589 inches of water with a 95% confidence. Equation 2.3 is used instead of simply adding two standard deviations to the tolerance limit, because it is assumed that any value between the true value and the tolerance limit is acceptable, requiring less than 2 standard deviations above the tolerance limit to provide a 95% confidence that the value adheres to the requirements [16].

The effect of temperature on the uncertainty can be found by using the following formula from manufacturers guidelines [17]:

$$U_{temp} = [0.025\% \text{ of cal. range} + 0.009\% \text{ of URL}] \text{ per } 50^{\circ}\text{F} \quad (2.4)$$

Where URL stands for "Upper Range Limit", and in this case is 1000 inches of water. The temperature is assumed to not vary by more than 50°F, and the uncertainty due to the ambient temperature is therefore:

$$U_{temp} = 0.025\%(280 \text{ inH}_2\text{O}) + 0.009\%(1000 \text{ inH}_2\text{O}) = 0.16 \text{ inH}_2\text{O} \quad (2.5)$$

To get the true instrument uncertainty, the above temperature uncertainty and the specification limit must be combined using equation 2.2 to get:

$$U_{LDP-6001} = \sqrt{SL^2 + U_{temp}^2} = \sqrt{(1.2 \text{ inH}_2\text{O})^2 + (0.16 \text{ inH}_2\text{O})^2} = 1.2690 \text{ inH}_2\text{O} \quad (2.6)$$

In order to get the final uncertainty of the data produced by LDP-6001, the uncertainty due to the electronics must also be taken in to account. The output signal from LDP-6001 separate from the pressure measurement is looked at first. A HARTTM communicator is used to send a signal from the output channel of LDP-6001 to the aforementioned Fluke 45 multimeter. The tolerance limit used in this calibration is 0.01 mADC, and the Fluke 45 uncertainty at 20 mADC is 0.013 mADC as previously discussed. Equation 2.3 is used to get a specification limit of 0.0266 mADC with a 95% confidence. Next the uncertainty due to the 4 to 20 milliamp input module, the last interface between the instrument and the final data, is calculated using a slightly different equation than 2.3.

$$SL = \sqrt{(TL + 2\sigma)^2 + U_c^2} \quad (2.7)$$

This calculation requires an addition of the standard deviation, σ about the tolerance limit, which is chosen as 0.05% of the range of 16 mADC, or 0.008 mADC. The U_c is the extended uncertainty of the calibration process. This gives an uncertainty of the entire electrical loop of 0.9145 inches of water. The electrical loop uncertainty (0.9145 inches of water) combined with the true instrument uncertainty (1.2690 inches of water) using equation 2.2 gives an uncertainty in the data of 1.6 inches of water with 95% confidence.

2.1.2 Uncertainty for Pressurized Vessel

Since LDP-6001 does not measure a pressurized vessel, this calculation is not relevant for these results. It is included as a comparison to what the uncertainty would be for a differential pressure instrument that would read a vessel with static pressure. The process for calculating the uncertainty of a differential pressure instrument that is measuring a pressurized vessel is very similar to the non-pressurized method. The static pressure that the instrument is exposed to adds an environmental uncertainty much like that caused by the ambient temperature effects. The additional uncertainty caused by static pressure is given by the manufacturer and is below:

$$U_{pressure} = [0.025\% \text{ URL} + 0.1\% \text{ of reading}] \text{ per } 1000 \text{ psig} \quad (2.8)$$

This uncertainty would be calculated, then combined with the uncertainty caused by the temperature effects using equation 2.2.

2.2 Gravimeters

A gravimeter is a device used to measure the local gravitational acceleration caused by the Earth, or any other appreciably large mass. It is essentially a specialized accelerometer measuring the acceleration caused by gravity with appropriate sensitivity. The first proposed design to measure a change in gravitational acceleration relied on the use of a known mass to produce a certain pressure in a volume of gas, described in Rodés [18]. With a change in the magnitude of the gravitational acceleration, the volume of the gas changes, and thus the gas volume measurement is related to the change in the gravitational force. In such a configuration, however, any change in the gas temperature would greatly impact the measurement accuracy. For practical applications, the gas temperature must be measured to an unrealistic certainty.

Another design, often used in geology, is known as a "spring-type" gravimeter. This meter depends on a mass being suspended on a spring attached to a non-moving surface. The spring stretches or coils back as the gravitational acceleration of the mass is affected by Earth's gravity. The measurement of the spring length is thus employed to quantify the gravitational acceleration based on Hook's Law, where the force applied to a spring is directly proportional to the change in length of the spring, multiplied by a proportional constant called the spring constant.

$$F = -kX \tag{2.9}$$

Where F is the restoring force, k is the spring constant, and X is the distance the free end of the spring was displaced from its relaxed position. This type of gravimeter is typically used for relative gravity acceleration measurements, since it measures change in gravitational acceleration relative to the standard value of the Earth [6]. The main disadvantage with the spring type gravimeter is the drift due to the mechanical aspects of the spring. Since the 1980's, the technique has been greatly improved with the incorporation of electrostatic feedback, allowing

for a drift correction. The measurement of the change in spring length has also been improved upon through the use of a pair of capacitive plates which builds up voltage as the mass approaches either plate. For greater accuracy, position detection of the mass using laser interferometry, [19] is the most common way to measure minute changes in the spring length, and is used in what is considered the standard spring type gravimeter, the LaCoste-Romberg gravimeter. Modern spring based gravimeters are accurate to a few μGal range, where Gal is the unit of acceleration with $1 \text{ Gal} = 1 \text{ cm/s}^2$. To understand the size of 1 Gal, the typical value for the gravitational constant, g , is 9.81 m/s^2 is equivalent to 981 Gal. The gPhone gravimeter, developed by MicroG-Lacoste, has a $1 \mu\text{Gal}$ ($1 \times 10^{-6} \text{ Gal}$) precision, with a linear drift of $16 \mu\text{Gal}$ per day, and is considered to be among the best spring based gravimeters commercially available [20] [21].

The most advanced type of gravimeter available commercially is the superconducting gravimeter (SG). A SG operates on a similar principle as a spring-type gravimeter, and it detects the change in gravitational acceleration of a known mass through the measurement of the change in the mass position [22]. In a SG, the mass is suspended by the interaction between the inhomogeneous magnetic field from an electrical current in a set of wires and the currents induced by the interaction of the magnetic field and a superconducting sphere [23]. The stability of the meter depends on the the repulsion of the applied magnetic field. The magnetic field is created by a current moving through two niobium wires coiled around a mass in a hollow space. Niobium exhibits superconducting properties when cooled below its superconducting critical temperature of 9.2 K [24]. After the wires are cooled to this temperature, they can be isolated from the rest of the electrical system and the electrical currents become "trapped" in a nearly zero resistive lose system. The mass, also made of niobium and typically a hollow sphere [6], is also cooled to the superconducting critical temperature, allowing it to repulse the magnetic field created by the wires. The superconducting sphere is made hollow to lessen the mass, and therefore lessen the strength of magnetic field required to suspend the sphere. A tiny hole is usually drilled through the sphere to allow pressures on the

inside and outside of the sphere to be at equilibrium. The wires are positioned in such a way that the current flowing through them creates a large enough magnetic field to lift the sphere. The top wire is located close to the axis of the center of mass of the sphere, while the lower wire is located slightly below the sphere. Figure 2.2 shows this configuration with an additional Feedback coil. The Feedback coil is used to show the linearity of the meter, by relating the current induced on the surface of the sphere by the feedback field, to the current induced the surface of the sphere by the levitation field from the upper and lower coils. This magnetic feedback force maintains the sphere in a constrained position [25]. The dashed red lines in Figure 2.2 show an example of what the magnetic fields surrounding the sphere could look like. The space containing the mass must be large enough to accommodate for changes in the location of the sphere due to changes in local gravitational acceleration. This relies on a well made detection system, a strong magnetic field, and adequate shielding. In modern gravimeters, the maximum distance between the capacitive plates and the sphere is approximately 1 mm [6].

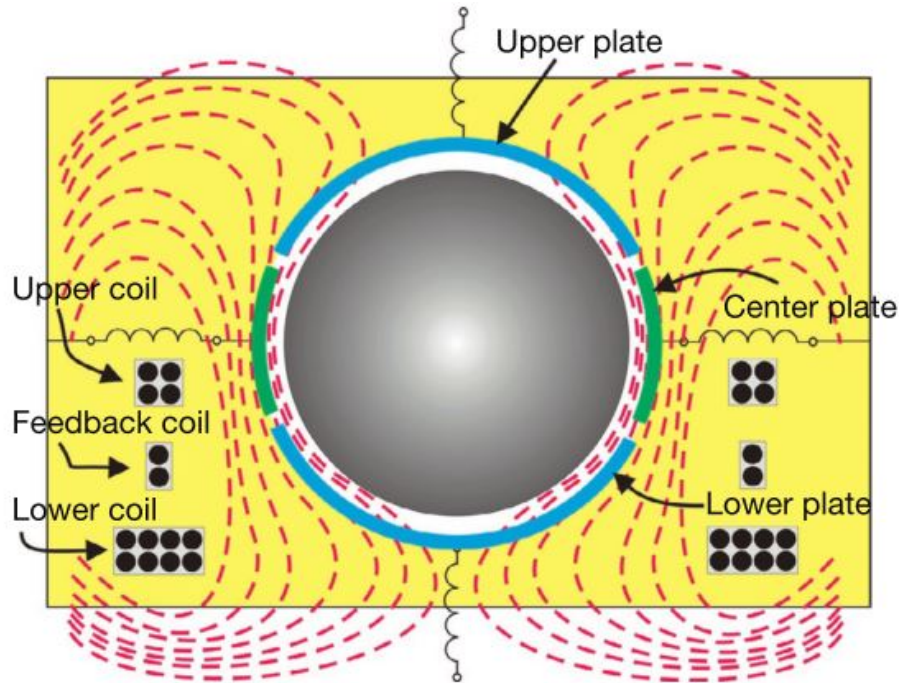


Figure 2.2: SG Sphere, Capacitive Plates, and Coil Configuration [4]

Similar to the capacitive sensing spring gravimeter, capacitor plates surround the levitating mass in all directions, providing very precise information on the location of the sphere in three dimensions. Two nearly hemispherical plates are placed at the top and bottom of the cavity containing the sphere, and a band shaped plate is placed around the center. With this configuration, any change in the location of the sphere greater than approximately 10^{-10} cm. will be detected [23].

Throughout the development of superconducting gravimeter systems, there have been some difficulties associated with their use. Since the superconducting critical temperature for niobium is much cooler than typical room temperature, a coolant system is required. The coolant used in the loop is typically liquid helium, which has a boiling point at room pressure of ~ 4 K [26]. Most SGs simply contain a

large volume of liquid helium in the dewer, without a refrigeration cycle. Once the liquid helium has evaporated and gained significant energy to cause fluctuations in data, the gravimeter is refilled. When this maintenance is required depends on the size of the dewer, and the tolerance of the fluctuations in the data. One of the earliest models created by GWR, Inc. was the TT30 SG. The device was installed in Royal Observatory of Brussels, Belgium in 1981, and had an internal volume of 200 liters filled with helium. This was required to be refilled every few weeks [6]. With the cost of liquid helium in the United States being around \$5 per liter [27], the cost to refill the meter was around \$1000 per week. However, this is most likely a low estimation, since the price of liquid helium in Germany and surrounding areas was much higher than elsewhere in the world [28]. Regardless of whether the meter has a refrigeration cycle, there must be thermal shielding. Because of the low temperatures involved, the thermal insulation is bulky and heavy, making transport of the gravimeter difficult. A SG must also be shielded from external magnetic fields to control the levitation of the sphere and keep contributions from external sources as small as possible. This also adds to the size and weight of the gravimeter. Another difficulty is the task of keeping the sphere stable as it is levitated. Since these instruments are designed to be very sensitive to minute changes in gravitational acceleration, any vibration of the gravimeter can have a severe impact on the signal. The combination of these drawbacks also brings another fault: the gravimeter must be available for maintenance to be performed regularly. The final, most daunting drawback to using gravimeters, is their cost. As mentioned earlier, SGs that do not have refrigeration systems must continually refill the liquid helium reserves, or the signal quality will degrade. Superconducting materials are expensive, and the device is new enough for there to be no mass production aspects, save for a few instruments which are a part of the overall system like thermocouples, or tiltmeters. The shielding mentioned earlier is expensive, and in most cases, must be made specifically for where the meter will be located. Many of the negative aspects associated with superconducting

gravimeters have been addressed and/or improved upon in the GWR iGravTM system.

2.2.1 iGravTM Superconducting Gravimeter System

The iGravTM superconducting gravimeter system is the most technologically advanced superconducting gravimeter system. Many of the disadvantages associated with superconducting gravimeters have been addressed with this system. For this experiment, GWR Inc. rented Oregon State University two iGravTM superconducting gravimeter systems. The systems included the superconducting gravimeters, each filled before being shipped with liquid helium, a computer for data collection, and the necessary connections in order to set up the meters. Figure 2.3 shows a GWR iGravTM SG system, including the superconducting gravimeter (blue), with baseplate and stabilizing feet (dark grey), attached to the cooling system (off white rectangle to right), and a data collection computer. All iGravTM systems consist of three main components: the dewer and baseplate, the cryogenic refrigeration system, and the control box and computer. The larger blue cylinder in Figure 2.3 holds the dewer, sensing equipment, including the superconducting sphere and wires, the capacitive sensing plates, the germanium thermocouple, the tilt meters, and heaters. All of the insulation and shielding is also contained by the blue cylinder, as well as the necessary parts of the coolant loop. The dewer is 40 inches in height and has a 36 inch outer diameter, allowing for an inner volume of 16 liters of liquid helium. With the sensor installed, the weight of the dewer is 65 lbs. [4]. Figure 2.4 shows a cross-sectional view of the inside of the dewer. Attached to the upper head are three stabilizing, noise dampening feet. These connect to the baseplate to give as stable a platform as possible for the upper head (smaller blue cylinder in Figure 2.3) to rest on, while still isolating the dewer from the vibrations caused by the cold head and electronics. The upper head connects the refrigeration system and other instrumentation to the dewer. The baseplate and thermal levelers are approximately 21.5 inches in diameter and weigh 16 lbs.

[4]. The next major component is the cryogenic refrigeration system used to keep the liquid helium below the critical temperature of the niobium in the system. The system consists of a Sumitomo SRDK-101D cold head, and a Sumitomo CAN-11C compressor, requiring a total power of 1.2 to 1.3 kW. The refrigeration system can operate between 4 and 38 °C [4]. In Figure 2.3, the refrigeration unit is the off-white rectangle with the red lettering to the right of the gravimeter. The figure shows the various connections required to complete the cooling loop. For this experiment, the refrigeration unit was not needed because the dewer could maintain a critical temperature environment throughout the experiment.

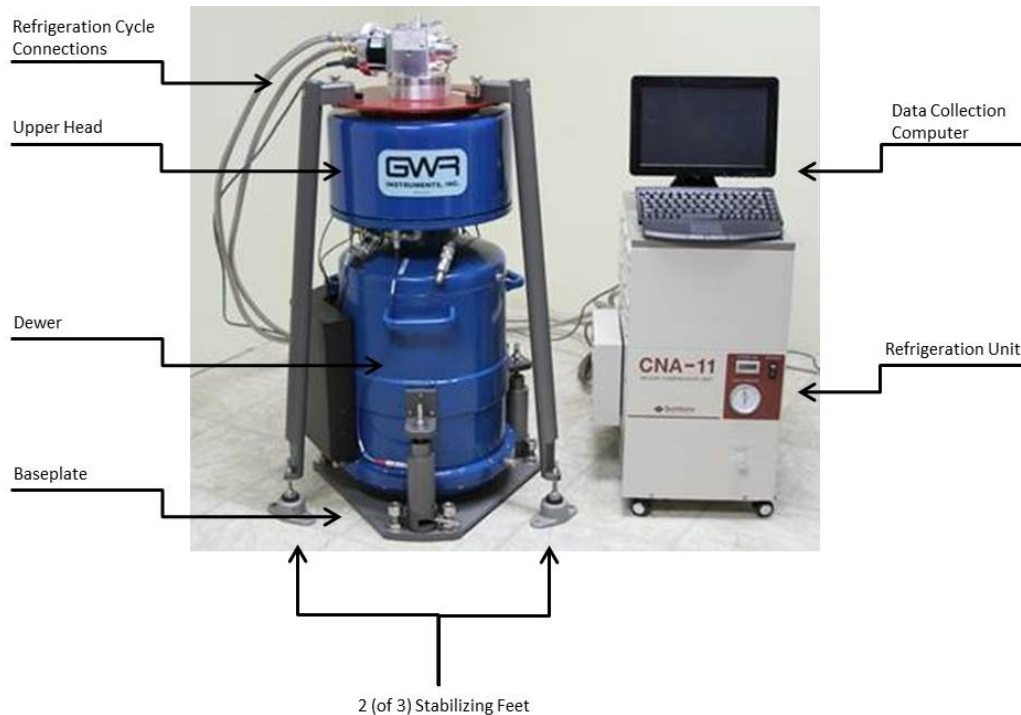


Figure 2.3: The iGravTM Superconducting Gravimeter System from GWR, courtesy of Dr. Richard Warburton of GWR [5]

The technological progression of electronics has allowed the gravimeter to be controlled remotely by putting the necessary electrical equipment in the upper head

of the gravimeter. In Figure 2.3, the smaller blue cylinder on top of the dewer holds the electronics, the refrigeration cycle cold head, and other instrumentation such as thermocouples and tiltmeters. The data collection computer (on top of the refrigeration unit) can easily be connected to the meter, but that is not required.

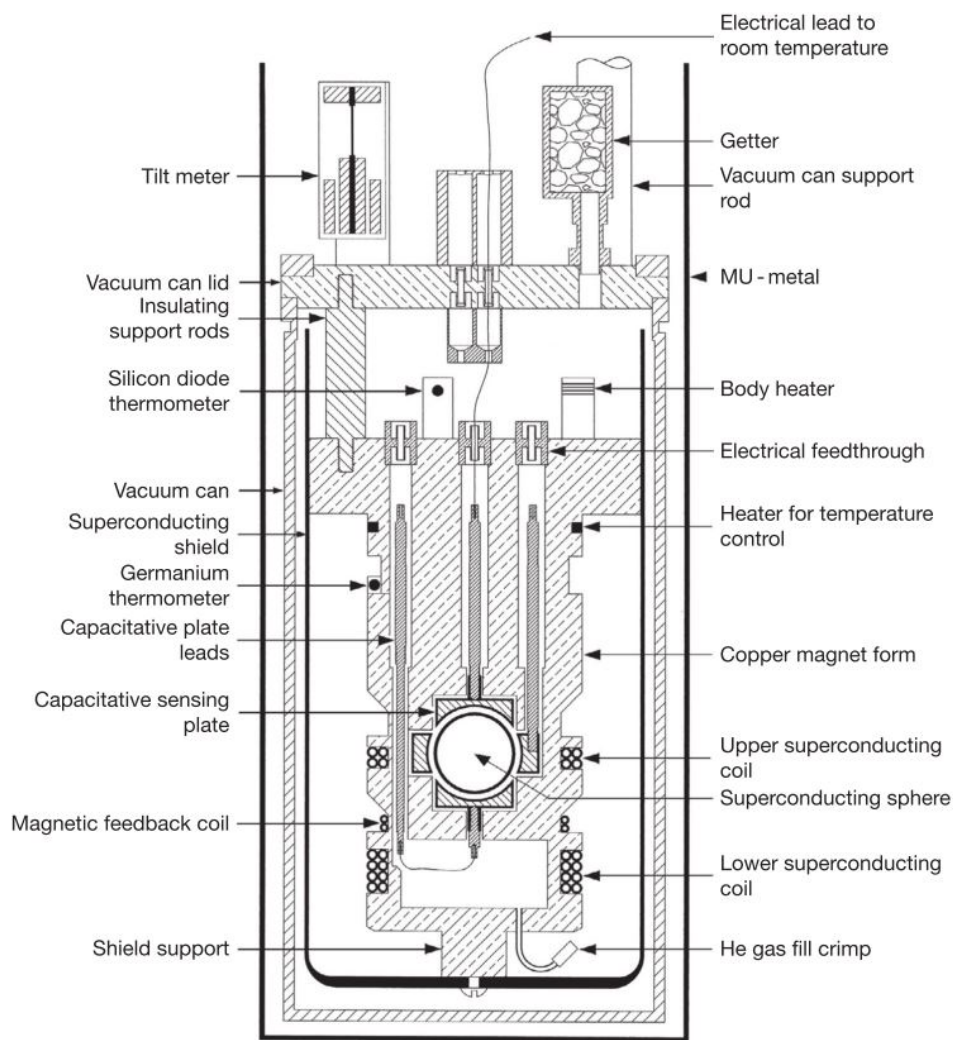


Figure 2.4: Cross-section of the iGravTM Dewer, [6]

The main improvements displayed by the iGravTM system [4] are:

- Smaller size, simpler configuration
- No consumption of liquid helium
- Able to move meter with sphere levitated
- Less expensive
- Less impact from noise
- Simpler operation and setup

Each of the improvements listed above are integral to the meters use in measuring liquid inventory in reactors, as explained below.

The first advantage that GWR's iGravTM system has over not only traditional spring based gravimeters, but other SGs as well is the systems size and configuration. From GWRs previous design to the iGravTM gravimeter, the dewer volume was reduced from 35 liters to 16 liters, the height of the dewer was reduced from 1.14 m to 0.82 m, and a very significant amount of weight was removed by replacing the thermal levelers previously attached to the sides of the dewer with smaller, lighter thermal levelers attached to the baseplate (the dark grey triangle under the blue dewer in Figure 2.3). Excluding the refrigeration system, the mass of the meter was reduced from 230 kg to 68 kg. With the refrigeration system, the total iGravTM system can operate easily within a 2 x 0.8 m area [6][29].

The next improvement integrated into the iGravTM system's design involves the liquid helium refrigeration system. Due to the requirement that the sphere and current supplying wires be maintained at temperatures at or below 4.2 K, a cryogenic cooling system is required [23]. The temperature of the sphere, wires, and shielding must be controlled to account for minute pressure changes (caused by storms, geographic location, etc.), humidity, and external temperature sources. The iGravTM system does this by utilizing a germanium thermocouple to sense the coolant temperature, and then will adjust the coolant temperature accordingly

using a series of heaters or the refrigeration loop. The dewer is also vacuum insulated, to inhibit convective heat transfer from external sources to the coolant. The dewer is insulated with high conductivity materials to insure as much temperature isolation from the environment as possible. With all of these components in place, the system temperature can be regulated to within a few microkelvin during operation [6]. This extreme temperature regulation helps with the instrument drift due to temperature variation which is typically seen in spring type gravimeters.

One of the driving design parameters behind the iGravTM system is that it must be as mobile ready as possible. This was done by making the system so well isolated to external influences that the system can be filled with liquid helium and the sphere can be levitated by GWR in San Diego, CA, then the meter can be shipped to its destination ready to set up. Even though there is less liquid helium in the iGravTM design than typical SGs, the system can be held in a configuration for a total of seven days without the temperature rising significantly enough to effect the system [29]. This was actually the method utilized for this experiment, and the set up time was greatly reduced because of GWR's work on the meter before it was sent to Oregon State University.

Another major advantage of the iGravTM system over traditional SGs is the cost. With the overall cost approximately half of previous SG models, the iGravTM system is much more economically feasible. Due to the reduced size, and material and instrument configuration, the cost of the iGravTM system is greatly reduced compared to other commercially available SGs [6][23].

Most of the improvements seen on the iGravTM system also reduce the effect of noise on the data from both external and internal sources [4]. The configuration of the three stabilizing legs and the baseplate isolates vibrations from the upper region of the meter, including the cold head and electronics. The interface between the neck of the dewer and the cold head is sealed with a rubber gasket, and stiff internal spokes connect the inner and outer walls of the dewer, producing much lower noise levels than observed in previous SGs [30][6]. The cryogenic refrigeration

system is able to be installed far enough away from the gravimeter that it does not contribute a meaningful amount of noise [6][31].

Another advantage implemented in the iGravTM system is the ability to monitor and control the meter remotely through an internet connection. Since the electronics fit above the dewer in a separate cylinder (just below the red disc in Figure 2.3), there is no need to have the data collection and control software in the same location as the meter, which is ideal for not only the typical use of these meters, which is often in remote locations, but for use in nuclear reactor liquid level measurements. Maintenance and configuration control of electronics is possible without having to have personnel close to the meter.

2.2.2 Superconducting Gravimeter Measurements

Measuring changes in the local gravitational field using superconducting gravimeters has been done commercially since the early 1980's [6]. Due to the high sensitivity of SGs, many different signals are detected which might not be desirable to measure. The observational signal directly from the gravimeter (after the signal in Volts is converted to Gal), is made up of solid Earth and oceanic tides, atmospheric noise, polar motion noise, instrumental drift, hydrological noise, and other smaller signals in addition to the desired data. The solid Earth and oceanic tide signal magnitudes are on the order of a few hundred μGal , and atmospheric pressure variations produce -0.3 to -0.4 μGal per mbar [32] [33] [34]. The hydrological noise contributions are usually much smaller, typically around 5 μGal each [6]. Noise due to polar motion is not accounted for during studies lasting less than a week, as they typically impact the signal by less than 0.01 μGal per day [6]. The instrumental drift is very specific to the model of SG, and in the case of this experiment is very small at around 0.5 μGal per month [4]. As explained by Mickus [7], the instrumental drift in gravimeters is very linear, as shown by Figure 2.5.

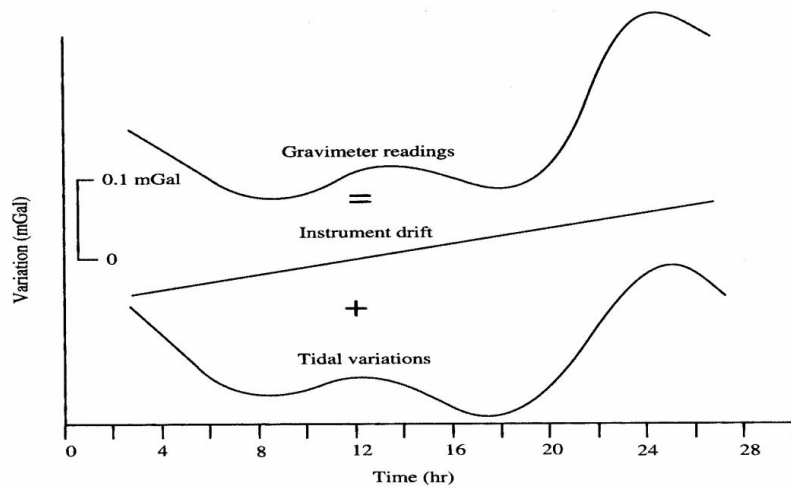


Figure 2.5: An Example of the Impact of a Linear Instrumental Drift, [7]

The drift of the gravimeter is accounted for by simply subtracting the known drift rate from the data set. For the purposes of this study, all aforementioned sources of noise must be filtered from the raw signal in order to characterize the NIST-1 facility as accurately as possible. Other noise factors arise based on the meters proximity to all of the other environmental factors, including external vibrations due to industrial facilities or vehicles. Ideally, SGs should be placed ~ 100 m or more from other instruments or heavy-traffic areas, and should pass the background seismometer noise test proposed by Peterson et al in [35] and [6] (page 70 and 71). Since there are so many different contributors to the signal, specific intervals of signal frequencies are looked at to minimize the dominant sources impact to the signal. All signals with frequencies higher than 0.02 Hz are dominated by oceans (micro-seismic signals), and all frequencies below 0.005 Hz are dominated by atmospheric and hydrological signals. Even while measuring within this band of frequencies, earthquakes and other noise can dominate. In order to accurately measure instrumental noise, the earth must be quiet, which is not possible during this experiment since the records are too short [5].

2.2.3 iGravTM Uncertainty Estimation

Each of the contributions to the iGravTM signal mentioned above must be accounted for in order to isolate the desired signal. This is done by simulating the oceanic tides, the solid earth tides, and the oceanic loading. The simulated signals are then subtracted from the raw signal taken by the SG. To calculate the instrument precision of a SG, the Power Spectral Density (PSD) of the gravity signal must be known. PSD relates the typical uncertainty of the meter to the frequency band it typically operates within. A typical PSD for SG is approximately $4 (nm/s^2)^2/Hz$ [5]. PSD is used to calculate the Limiting Precision (LP), and is based on the gravity signal with the tides and atmospheric signals subtracted out. The LP is the uncertainty of the meter for a specific signal frequency. The manufacture's brochure for the iGravTM SG claims a precision $0.05 \mu Gal$ in the time domain for 1 minute averaging [4]. This was calculated using the equation for LP as described by Crossley, et al in [8]:

$$LP = \sqrt{\frac{PSD}{T_{obs}}} \quad (2.10)$$

Where PSD is the Power Spectral Density, T_{obs} is the filter time (on the order of minutes to hours), and LP is the limiting precision. The PSD is the fluctuation of the instrument per sampling frequency in Hz (Gal^2/Hz). Typically, this value is found by characterizing the noise of the environment where the gravimeter will be located. Raw data will be taken for an length of time typically greater than a month, then the tides will be simulated and removed from the data, and nominal atmospheric pressure effects will also be subtracted [8]. A 9 degree polynomial fit to the the data is subtracted to remove any residual tides, and the 5 quietest days with the smallest variation are selected. The PSD and its mean value between 340 and 600 second intervals are calculated. The following figure shows the resulting plot of PSD vs. frequency of event for not only the iGravTM system, but other well known gravimeters.

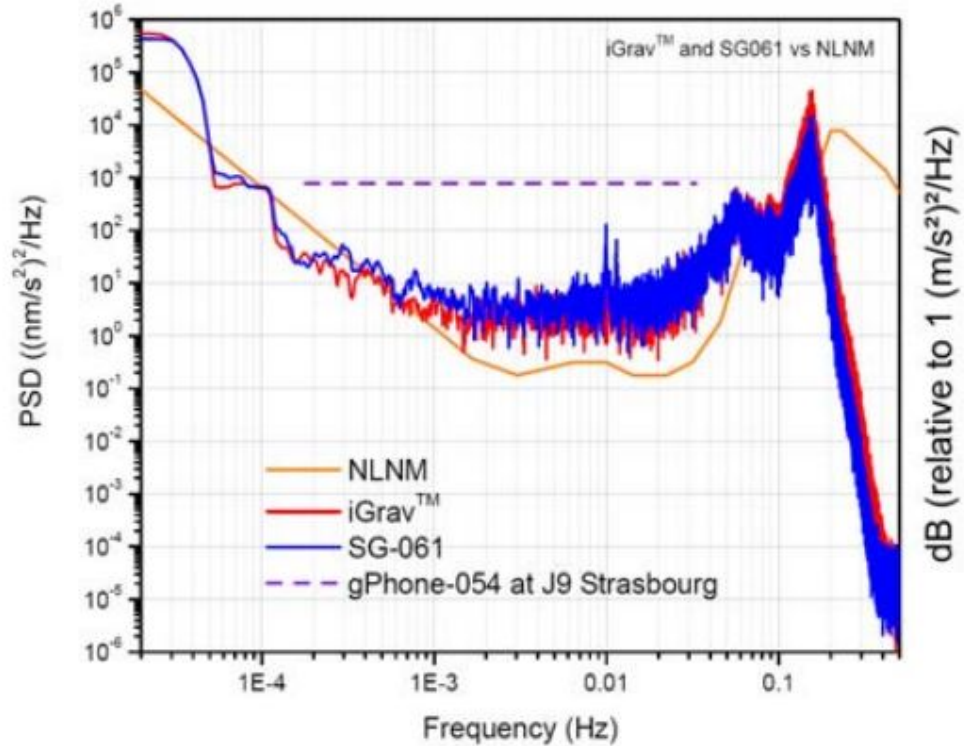


Figure 2.6: PSD $((nm/s^2)^2/Hz)$ vs. Signal Frequency (Hz) for Various Gravimeters [8]

Oceanic tides are simulated using TSoft, a software program which is standard in geophysical experiments. Section 4 of the TSoft Manual [36] describes how this is done. The uncertainty associated with the oceanic tidal simulation is 0.6 nm/s^2 , according to [37] and [38]. The solid earth tides are calculated using a program called ETERNA [39]. The version used in this study is the most recently available version, 3.30. The accuracy of this program is approximately 1 nanoGal [39]. The ocean loading correction accounts for the changing ocean location due to the tides. This is simulated using H.G Scherneck's ocean loading program [34]. The location of interest is input and various ocean tide models can be selected. A full description of each of the models can be found at H.G. Scherneck's website, [40]. The accuracy of the ocean loading simulation is at worst 2 to 5 %, according

to [6], [41], and [42]. This accuracy was found by simulating multiple locations that are well known to produce steady, repeatable data. One of the factors which impacts the ability of the simulation to accurately predict ocean loading is the distance from the measurement site to the coast. The closer the site is to the coast, the more difficult it is to simulate the ocean loading effect on the measurement. Measurement sites within approximately 150 km. can produce even greater errors [42] [41]. This makes it difficult to characterize the uncertainty with this simulation, as the testing site at Oregon State University is easily closer than 150 km. to the Oregon coast. Assuming a 5% uncertainty, this translates to approximately 0.2 μGal uncertainty for the ocean loading simulation. The impact of the inaccuracy of the ocean loading simulation may cause some difficulties with the measurements performed at the Oregon State University testing facility.

Once each of the contributions to the signal mentioned above have been subtracted from the data, the uncertainty from each simulation must be carried through to the final signal. This was done by utilizing the propagation of error equation below:

$$\sigma_f = \sqrt{\left(\frac{\partial f}{\partial x}\right)^2 \sigma_x^2 + \left(\frac{\partial f}{\partial y}\right)^2 \sigma_y^2 + \dots} \quad (2.11)$$

Where σ_f is the uncertainty of the combined data, and σ_x, σ_y are the uncertainties of the individual signals. Since the signals are being subtracted from the original data, f takes the form: $f = w - x - y - z$, where w is the raw instrument data signal, x is the oceanic tidal simulation signal, y is the solid earth tidal simulation signal, and z is the simulated ocean loading correction signal. Utilizing Equation 2.11, the estimated uncertainty after the data has been filtered of simulated tides and ocean loading with the superconducting gravimeters is therefore approximately 0.201 μGal . This clearly shows that the dominant source of uncertainty comes from the ocean loading simulation. It should be stated that the ocean loading uncertainty is an assumption, and the data from this experiment

shows that there is some likelihood of it being greater than the 5% used in this calculation.

The uncertainty when subtracting the signals from multiple iGravTM gravimeters can be found much more simply. If two gravimeters are in relatively the same geographic location, any of the larger environmental noises, such as those mentioned earlier, are captured by both meters. The subtraction of their signals eliminates any shared signals and the remaining signal would be from any local event. This method should produce a lower uncertainty and more accurate signals in the case of this experiment since the time to characterize the environmental noise is too short. To calculate the uncertainty of this signal, the instrumentation uncertainty, in this case the limiting precision, of each gravimeter is combined using equation 2.11. The limiting precision for each of the iGravTM gravimeters used in this study were approximately 0.018 μGal , therefore the uncertainty associated with the subtraction of one signal from the other is estimated at 0.025 μGal .

Chapter 3: Methods

3.1 Simulation

This section covers the theory concerning the simulation that was developed by Dr. Ridgway from Information Systems Laboratory, Inc. (ISL) and how it was used to predict signal strength of the gravimeters seen from NIST-1 facility. One of objectives of this study was to model what a gravitational acceleration signal given by a nuclear reactor vessel would look like during various conditions, including normal operations and accident scenarios. The purpose of the simulation is to accurately predict the signal strength seen by an observation point next to a known volume. This was done by utilizing the finite volumes method to split the volume of interest into smaller differential pieces, and summing the gravitational effects of each piece on a specified location relative to an observation point. The following section describes the method for developing the simulation used to model a cylindrical volume of water.

The force of gravitational attraction between two masses can be expressed by Newton's Law of Universal Gravitation:

$$\vec{F}_{12} = -\frac{Gm_1m_2}{(r_{12})^2}\hat{r}_{12} \quad (3.1)$$

Where the gravitational force between two masses, \vec{F}_{12} , is equal to the mass of each object, (m_1 and m_2) multiplied by the gravitational constant, ($G = 6.674 \times 10^{-11} \frac{Nm^2}{kg^2}$) and divided by the square of the distance between the two objects, r_{12} . The distance from mass 1 to mass 2 is $r_{12} = |\vec{r}_2 - \vec{r}_1|$, and \hat{r}_{12} is the unit vector along the distance between the two objects defined as:

$$\hat{r}_{12} = \frac{\vec{r}_2 - \vec{r}_1}{|\vec{r}_2 - \vec{r}_1|} \quad (3.2)$$

In our experiment, of interest is how the stationary mass in the gravimeters will be impacted by a changing volume of water some distance away. Since the mass of the water volume is changing, a differential volume method is used to allow each differential volume to have a discrete location relative to the mass in the gravimeter. The acceleration that the mass in the gravimeter (i.e. mass 2) undergoes due to the mass of interest (mass 1) is found by substituting Newton's Second Law of Motion, which states that any force is equal to the time rate of change of momentum, in to Equation 3.1:

$$\vec{F}_2 = m_2 \frac{d\vec{v}}{dt} = m_2 \vec{a}_2 \quad (3.3)$$

Setting Equation 3.3 equal to Equation 3.1, the acceleration experienced by mass 2 from the gravitational force of mass 1 is:

$$\vec{a}_{21} = -\frac{Gm_2}{|r_{12}|^2} \hat{r}_{12} \quad (3.4)$$

Using the differential volumes method, the effect of each differential mass is summed. This gives:

$$\begin{aligned} \vec{a}_{21} &= -\int \frac{Gdm_2}{|r_{12}|^2} \hat{r}_{12} \\ &= -\int \frac{G\rho_{i,2}dV}{|r_{12}|^2} \hat{r}_{12} \end{aligned} \quad (3.5)$$

This equation accounts for each individual differential volume's density as $\rho_{i,2}$, meaning that there are i differential volumes, with location related to mass 2. In

our test of the simulation, a cylindrical tank will be used, therefore, the gravitational force will be summed in cylindrical coordinates, as shown below:

$$\vec{g}_{21} = - \int_{z_1}^{z_2} \int_{\theta_1}^{\theta_2} \int_{r_1}^{r_2} \frac{G\rho_{i,2}}{|r_{12}|^2} \hat{r}_{12} r_{12} dr d\theta dz \quad (3.6)$$

Here, the acceleration term \vec{a}_{21} , has been replaced with a more standard variable representing the acceleration due to gravity \vec{g}_{21} . In order to perform the integration in a timely manner over the volume of interest, each integral operation is approximated by a summation of the differential volumes. A height and radius of the volume to be measured is chosen by the user. The units of these parameters can be in any unit of length, as long as they are the same. They are typically entered in meters, and the cylinder will always be centered on the origin. Modifications have been made to the code to allow the user to input the cylinder location relative to the origin, but it was not utilized in this study. Next, the number of points along each direction in cylindrical coordinates is chosen. These will define the number of pieces the volume will be broken in to, i.e. if the user chooses N points along the radial direction, there will be $N - 1$ slices along the radial direction. The user also defines the position(s) of the observation point(s), again starting from the origin, in cartesian coordinates. The simulation allows any number of observation points in any direction, as long as the observation points are located outside the volume of interest. For example, with a cylinder of interest with radius of 1 m, and a height of 2 m, the observation points must be either farther than 1 m horizontally or 2 m vertically from the origin. The density is also specified by the user, and can be a single value (as was done to simulate the NIST-1 CPV), or an array equal to the number of differential volumes. Another script is run that takes the volume of interest parameters, and defines the differential volume dimensions, as well as the position vector for the center of each differential volume from the origin. An equivalent spherical radius is calculated using the average distance from the average differential volume. This is used to check the location of the observation points against the volume of interest. The simulation is terminated

if the observation points are located within the volume of interest. A final script calculates the gravitational acceleration experienced at the observation point in cartesian coordinates. In this study, the change in gravitational acceleration along the vertical (z) axis is the most interesting parameter, and will be reported in Chapter 4.

In order to ensure that the simulation output is accurate, the minimum number of points along each axis must be defined. A sensitivity study was performed on the simulation to quantify the change in magnitude of the signal as the number of points along each axis change. This was done with a constant volume, the volume used to simulate the CPV, in order to quantify the minimum number of points along each axis for the largest volume to be looked at. The NIST-1 CPV has an inner diameter of $40 \frac{1}{4}$ inches $\pm \frac{1}{8}$ inches, a wall thickness of $\frac{1}{4}$ inches $\pm \frac{1}{16}$ inches, and will be filled to a maximum of 255 inches $\pm \frac{8}{5}$ inches with city water. The outer diameter of the dewer on the iGrav system is 36 inches, therefore, the closest that the sphere can be to the center of the water column is $20 \frac{1}{8} + \frac{1}{4} + 18 = 38 \frac{3}{8}$ inches. Utilizing the error propagation equation (Equation 2.11), the uncertainty associated with this horizontal distance is 1.61 inches. It was assumed that the sphere of the gravimeter rested at the same elevation as the lowest point of the water column. The location of the observational point in order to calculate the minimum required number of points in cartesian coordinates is ($38 \frac{3}{8} \pm 1.61$ inches, 0 inches, 0 inches).

The number of points required along the z -axis was looked at first. The number of necessary points along the z -axis was quantified by running the simulation for the CPV with an arbitrary number of points in the r and θ directions (10 and 20 respectively), then varying the number of points along the z -axis from 1 to 75. The change in signal between each change in the number of points along z , was calculated by subtracting the previous signal from the current signal. Figure 3.1 shows how the signal varies as the number of points along the z -axis increases.

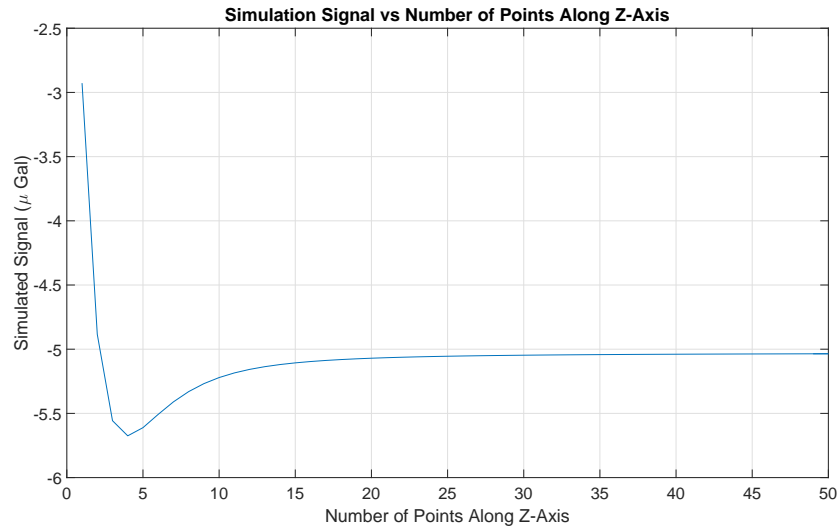


Figure 3.1: Simulation Sensitivity to Changing Number of Points Along Z-Axis

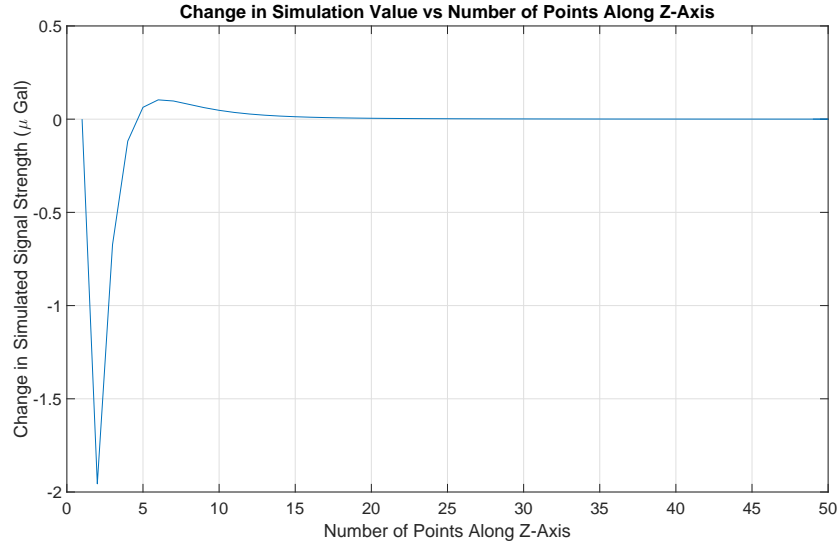


Figure 3.2: Difference in Simulation Signal with Changing Number of Points Along Z-Axis

After roughly 25 points along the z-axis, there is little change in the simulated signal strength. Since the accuracy of the iGrav system is approximately $0.018 \mu Gal$, the change in signal between points along an axis must be at least lower than this value. To ensure there is no impact on the simulation results, a change in signal of less than 1 order of magnitude of the uncertainty ($0.0018 \mu Gal$) was chosen to designate the minimum points along that axis. Using this criteria, a minimum of 28 points along the z-axis must be chosen to ensure minimal effect on simulation results.

Sensitivity studies were also performed on the impact of the number of points along r and θ . For the r-axis sensitivity, the number of points along the z-axis was held at 28, and the number of points along θ was held at 20 points. The number of points along r was varied from 1 to 150. Figure 3.3 shows how the signal changes with changing points along each of those dimensions.

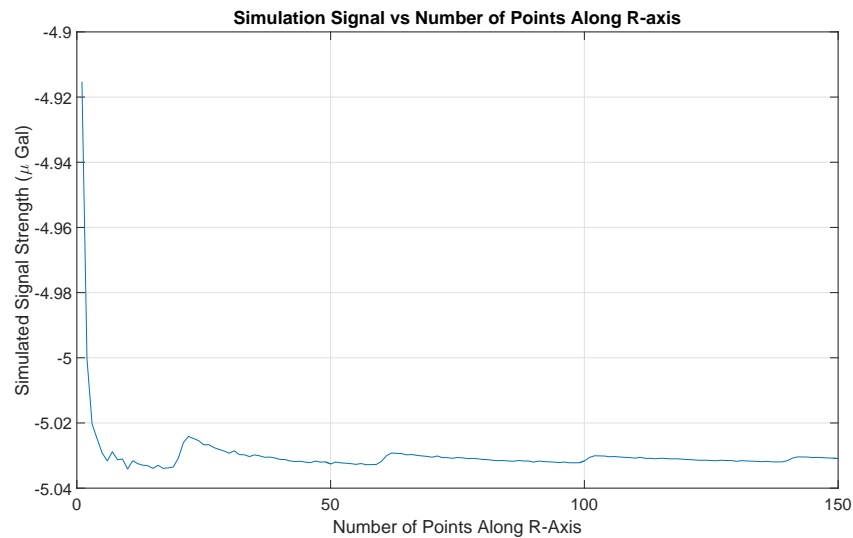


Figure 3.3: Simulation Sensitivity to Changing Number of Points Along R-Axis

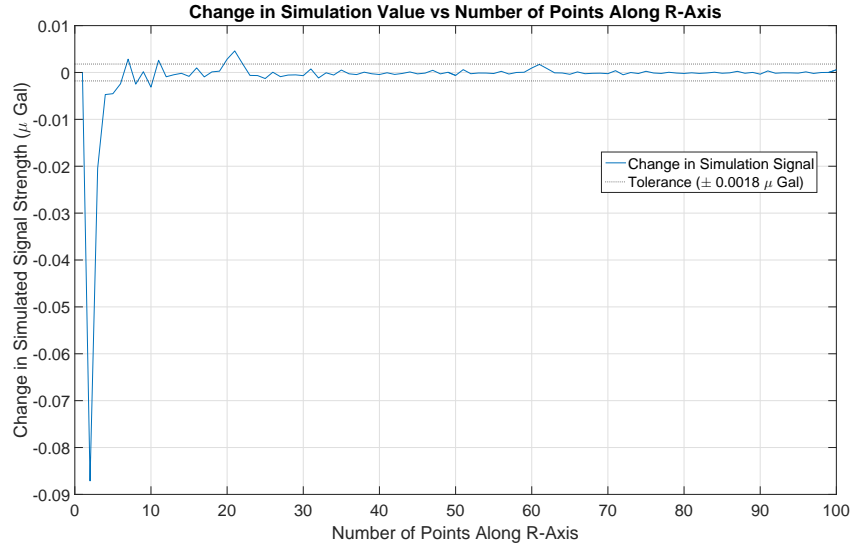


Figure 3.4: Simulation Sensitivity to Changing Number of Points Along R-Axis

Figure 3.4 plots the difference between each simulated signal as the number of points along the r-axis increases. Using the same criteria for the r-axis that was used for the z-axis, a minimum of 62 points along the r-axis are necessary to ensure the simulation does not vary significantly with points along the r-axis.

A final sensitivity study was performed on the effect of changing the number of points along the θ -axis has on the simulated signal. This time, the number of points for the z-axis and r-axis were held constant at 28 and 62 respectively, and the number of points along the θ -axis was varied from 1 to 50. Figure 3.5 shows how the simulated signal changes, and Figure 3.6 shows the difference in the simulated signal, as the number of points along the θ -axis changes. Once again, holding to the same standard used for the z-axis and r-axis, the minimum number of points along the θ -axis is 22.

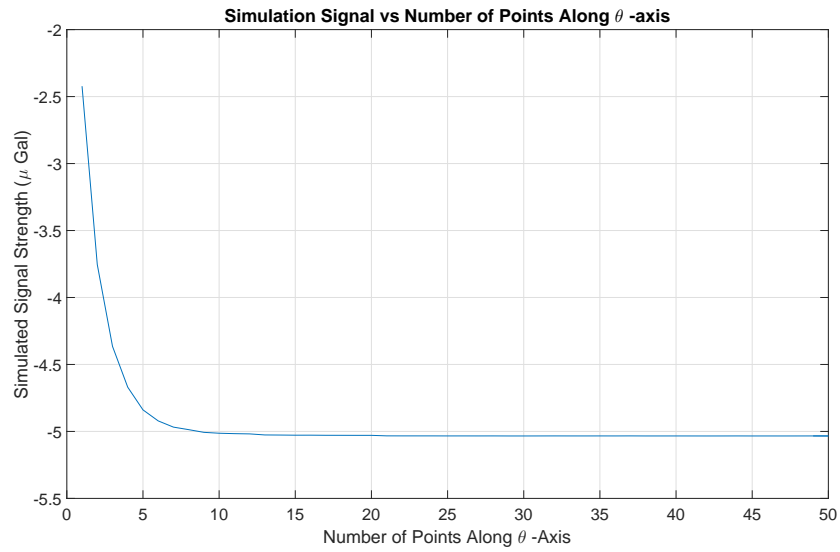


Figure 3.5: Simulation Sensitivity to Changing Number of Points Along θ -Axis

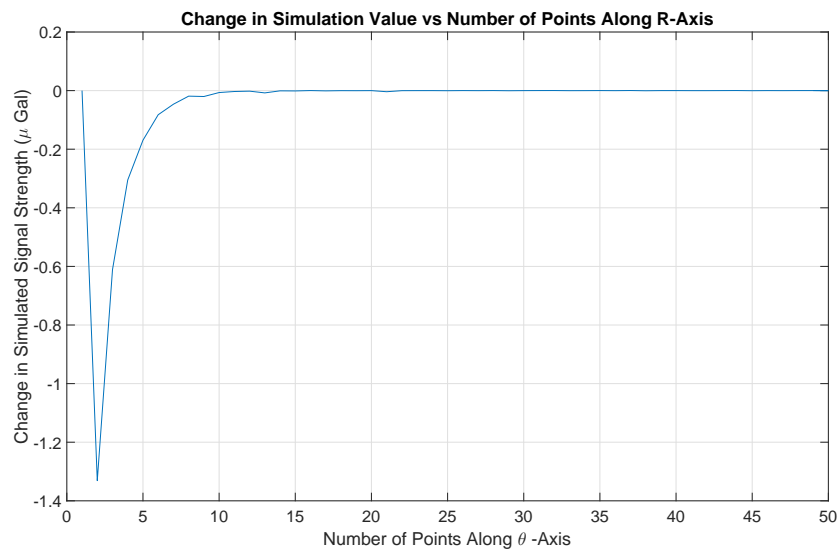


Figure 3.6: Simulation Sensitivity to Changing Number of Points Along θ -Axis

The observational points in the CNV simulation were varied from the bottom of the lower cylinder, to the top of the upper cylinder. The observation points were placed as close to the respective cylinder as possible as the elevation was changed. This ensured that the largest signal was found at the appropriate observation point.

3.2 Experiment

In order to meet the objectives of this study, the NIST-1 facility was chosen to be characterized by two iGrav systems. This was done to allow a variety of data to be taken simultaneously from different locations in the facility. In this section, the NIST-1 facility will be described. How each vessel was handled in the simulation will also be discussed. An overview of the data collection procedure used in this study will also be presented, including an outline of the current method of measuring level with a differential pressure meter, the configuration of the iGrav systems, and how the CPV level was manipulated.

3.2.1 NIST-1 Facility Description

The NIST-1 facility is a scaled thermal hydraulic, integral and systems testing facility. Unlike the NuScale prototypical design, the NIST-1 facility is made of three vessels which are not surrounding each other, in order to provide accurate instrumentation on how the system behaves in various accident scenarios. The RPV and secondary system are coupled together as in the prototype, but the containment vessel does not surround these systems. They are instead connected through various piping with the same purposes as in the prototype design. The CNV is also not surrounded by a large pool of water, but is instead connected to a cooling pool vessel (CPV), by a heat transfer plate.

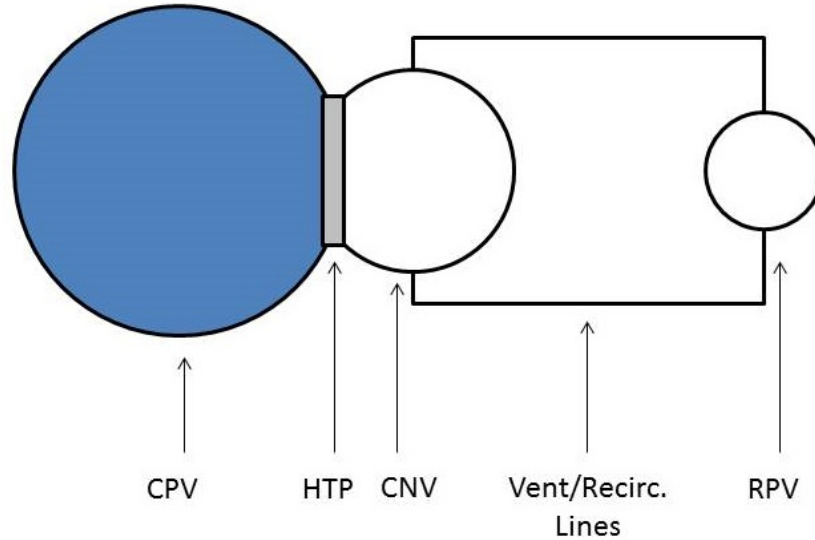


Figure 3.7: Overhead View of NIST-1 Facility, I made

A top-down view showing the layout of the three vessels, the piping, and the heat transfer plate is shown in Figure 3.7. Each of the vessels will be described in more detail in the following sections.

3.2.1.1 Reactor Pressure Vessel

The RPV at the NIST-1 facility is geometrically similar to the NuScale prototypical design. The RPV has a core which consists of electric heater rods at the bottom of a coolant riser section. At the top of the riser is the pressurizer, which controls the pressure of the primary system with a bubble of superheated steam. The pressurizer is separated from the primary loop by a baffle plate, and the steam bubble is controlled with electrical heater rods. The baffle plate turns the primary coolant flowing out of the riser section back down around an annular outer path between the vessel wall and the outside of the riser section. Here, the coolant passes against a helical coil steam generator, which has approximately room temperature water

flowing through by way of the main feed pump. This steam generator changes the density of the primary coolant, by allowing energy to transfer between the hotter primary coolant and the cooler secondary coolant in the steam generator. As the temperature of the primary coolant lowers, the density changes, providing a section of more dense fluid. With correct operation, the density difference between the coolant leaving the core, and the coolant after the steam generator provides the driving force of the primary coolant flow. One of the main differences between the NIST-1 facility and the prototype is that the NIST-1 does not have fission inducing fuel in the core. The heat that would be generated by a typical core is provided through electrical heater rods, which are controlled to behave as the prototype would during steady state and decay heat scenarios. This allows the NIST-1 facility to provide scenarios mimicking the same temperatures and pressures as the prototype would experience. Despite this similarity, there is less volume of coolant in the primary system in the NIST-1 facility compared to the prototype design. Since the gravimeters under investigation respond to the gravitational force which impact it, and the gravitational force is a function of the mass in the vessel being measured, the signal strength expected to be given off by the RPV is much less than that given by the other two vessels on the NIST-1 facility. The geometry is also not cylindrical, and since the simulation was written with cylindrical coordinates, significant modifications to the simulation would need to be made in order to characterize the RPV. This will be discussed further in Section 5.2: Future Work.

3.2.1.2 Containment Vessel

In the NuScale SMR design, the containment vessel completely encloses the main systems of the reactor, including the primary loop, the steam generator, and the pressurizer. The containment vessel for the NIST-1 facility (CNV) does not enclose the reactor pressure vessel as it would in the NuScale power plant design. Instead, various safety system piping lines, which are a part of the full scale design, are also

scaled and connect an external CNV to the RPV. Orifices are put in place along the lines in order to mimic pressure drops which would be experienced in the full scale design. In an accident scenario requiring a blowdown from the RPV in to the CNV, the valves would be automatically actuated, completely taking human intervention out of the equation. This accident scenario is exactly what the NIST-1 facility was built to simulate. During an event like this, the core is automatically tripped in to decay mode, meaning that some residual energy is being emitted in to the coolant. The upper relief valves are opened, to allow the super heated steam to enter the CNV, while not exposing the core region. The larger volume of the CNV, and the heat transfer plate attaching the CNV to the large, cool volume of water in the cooling pool vessel (see next section), causes the steam to condense. This condensed steam collects at the bottom of the CNV. Once enough steam has condensed, recirculation valves are opened to allow the now saturated liquid to flow back in to the primary system to continue cooling the core. This type of accident scenario is exactly what must be able to be detected in order for the iGrav system to be relied upon to measure liquid level for the NIST-1 reactor.

As with the RPV, the total volume in the CNV was characterized using room temperature water to completely fill the vessel, and then the water was drained out and weighed. This gave a total volume of 27.1 ft.³. The CNV was approximated as three cylinders with various outer radii stacked on top of each other. Each of the three cylinders dimensions for the simulation were chosen to maintain the volume found above, and to keep the geometry as similar as possible to the actual facility. The first cylinder was approximated as being 4.114 ft. (1.254 m.) tall with an outer radius of 0.793 ft. (0.242 m.). The second cylinder was approximated as being 13.133 ft. (4.003 m.) tall with an outer radius of 1.265 ft. (0.386 m.). The upper most cylinder was approximated as being 3.857 ft. tall (1.175 m.), with an outer radius of 1.652 ft. (0.503 m.). Using room temperature water at ambient pressure, the density of the fluid in the CNV for the simulation was calculated to be an average of 62.36 lb/ft.³ (999 kg/m³). Using these parameters, the volume of the simulation of the CNV is approximately 26.3 ft.³, approximately 3% less than

the actual vessel. This configuration is similar to the heights and diameters of the actual CNV, and also preserves the majority of the volume the gravimeter would be able to detect.

3.2.1.3 Cooling Pool Vessel

The cooling pool in the Nuscale prototype design is a large pool of room temperature water in which the modules will be contained. The purpose of this pool is to remove heat from the module during a breach of the RPV, where primary coolant is leaking in to the containment vessel. The hot coolant would transfer energy to a cooler pool through the containment wall, allowing it to condense back in to liquid water. This liquid would then be transferred back in to the RPV to continue cooling the core, creating a natural circulation loop. The cooling pool is large enough to absorb a lot of the energy from the leaked coolant, and vent it to atmosphere conditions without any release of coolant in to the pool. On the NIST-1 facility, the cooling pool is modeled as a large, nearly cylinder vessel coupled to the CNV by a heat transfer plate. The plate connects one side of the CNV to the cooling pool vessel (CPV), allowing the heat transfer between the pool and the containment to be scaled correctly. The CPV sits on the floor of the facility bay, and is open to atmospheric conditions at the top. There is a gap of 24 13/16 in. from the floor to the base of the water column contained by the CPV. Unlike the CNV, the inner radius of the pool can be approximated as constant at 20 1/8 in. \pm 1/8 in. throughout the height of the vessel. The maximum water height, for the purposes of this experiment, is approximately 255 inches from the bottom of the water column, or 279 1/8 in. from the facility floor. The cooling pool is able to be filled of room temperature city water, simply by the city water pressure, which is controlled by a valve at the bottom of the vessel. The CPV can be drained by way of two drain lines, one being larger than the other. Since the vessel is approximately a cylinder, no modifications were made to the dimensions in the simulation. As was done in the CNV, the CPV volume was characterized

by draining and weighing water from the vessel by NuScale, Inc. The simulation volume and the as-found volume agree to within approximately 1.5 ft.³, or about 1%. Using room temperature water, the maximum signal which would be seen by the iGrav system according to the simulation would be approximately 5.6 μGal .

3.2.2 Current Level Measurement

The method used to measure the liquid level in all vessels of the NIST-1 facility involves the use of a differential pressure meter. The vessel to be measured has two taps located at typically the vertical top and bottom of the vessel, where the pressure at each location is measured using a diaphragm attached to a capacitive sensor. For this experiment, the signal seen by the gravimeter was compared to the liquid level which was measured using a Rosemount differential pressure meter, specifically a 3051S model, designated as LDP-6001. The meter was calibrated between 0 and 280 inches of water (inH₂O), and has a data uncertainty of about 1.6 inH₂O. Figure 3.8 shows the distance between the upper and lower taps and the instrument configuration of LDP-6001 during the experiment. The figure also shows the elevation change between the lowest point of the CPV and the upper tap (275 inH₂O). The difference between the two elevation changes is 3 inH₂O. The distance between the lowest point in the CPV and the low sensing diaphragm is 3.9 inH₂O. This difference between the low point of the meter and the low point of the CPV is accounted for in the instrument's field range of -3.9 inH₂O to 271.9 inH₂O. This range allows the meter to read a 3.0 inH₂O signal when the elevation of the CPV is at or lower than the lowest tap elevation. This difference is therefore accounted for in all CPV level measurement data from LDP-6001. However, this results in a minimum signal seen by the simulation of the individual event data which is not 0 μGal . The simulation for each event utilized the CPV level data from LDP-6001 to calculate the expected signal from the gravimeters. This can be seen in the figures in Section 4.5, as the minimum value for the simulated signals is not 0 μGal , but approximately 0.1 μGal .

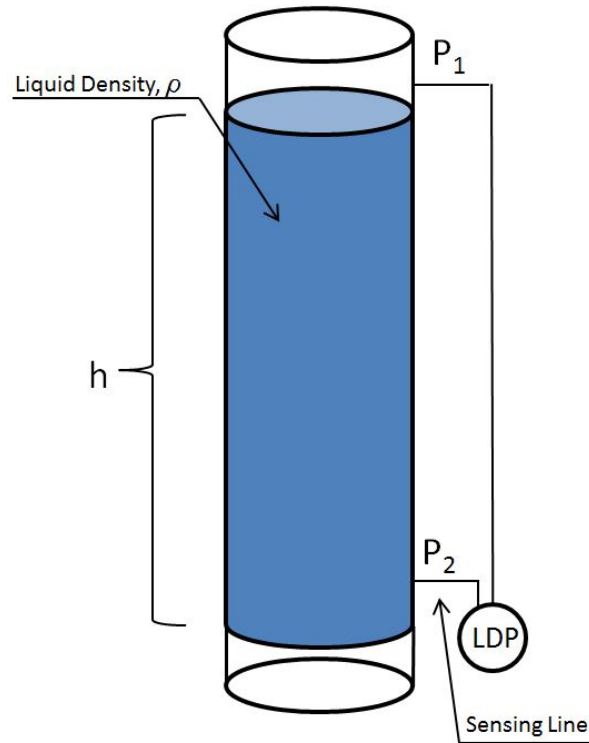


Figure 3.8: Configuration of LDP-6001 during Experiment

3.2.3 iGrav System Configuration

Throughout the experiment, the iGrav gravimeter system was set up in various locations in order to provide data to be compared to the simulation. The first gravimeter, designated as G03, was located at the base of the south side of the cooling pool, as close as possible to the vessel. It remained in this location throughout the duration of the experiment, as this was clearly the most stable position for the gravimeter. As shown in Figure 3.9, the gravimeter was 41 1/8 inches from the outer most radius of the CPV, and sat on the ground floor of the facility. The elevation change between the bottom of the water column and the sphere was

approximately 16 13/16 inches. A table was set up next to the meter to hold the data collection and gravimeter control computer and cables.

The second gravimeter, designated as G13, was moved around the facility a total of four times. Each location was chosen in order to show a variety of signals, attempt to find the most stable configuration, and to characterize the background signals. The first location was at the top of the CPV, on a metal grated platform which sits above the top-most water level above the vessel. Since the three stabilizing feet of the gravimeter require direct contact with the platform to be stable, this location was not ideal due to the grated floor. Since the CPV is a free standing vessel, any vibrations causing the vessel to move are amplified at the top and cause additional noise on the gravimeter. As discussed in Section 4: Results and Discussions, this location was not ideal so the gravimeter was moved after the first event. The second location was next to the side of the CPV, on the structure supporting the RPV. Since this structure was more stable, the signal seen by the gravimeter was better, but during the testing, the gravimeter was not allowed to come to a stable position after it was moved from the first location. The gravimeter was also placed next to other instrumentation and their sensing lines, which may have added noise to the signal. The next position for G13 was as far away from the CPV as possible, while still being inside the facility. The gravimeter was placed in this position in order to characterize the site background noise. The last location was very similar to the second, as we had realized that the signal from the second location was not as good as it could have been. This time, the most stable configuration for the gravimeter was found, and therefore some of the least noisy data was captured. Table 3.1 displays the distances of all locations of both gravimeters relative to the bottom of the center of the CPV. These were the dimensions used in the simulation to produce the results in Section 4.5.

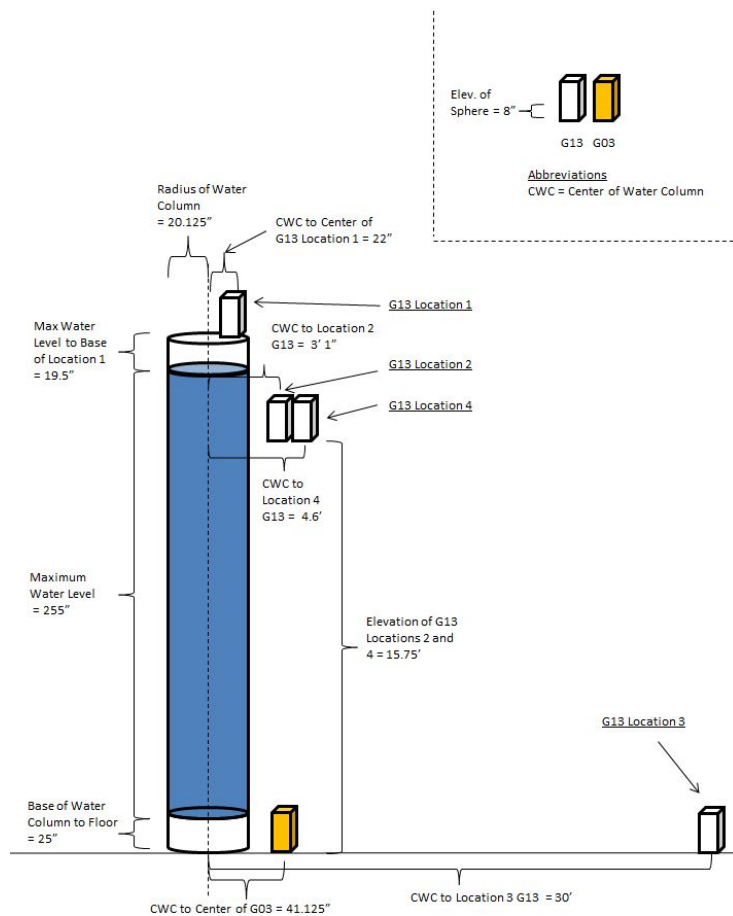


Figure 3.9: iGrav 03 and 13 Location Dimensions

Table 3.1: Gravimeter Locations

Gravimeter	Position Number	Event Number	x	y
G03	all	1-6	41.125	17"
G13	1	1	282.5"	22"
G13	2	2	37.2"	208.8"
G13	3	3 and 4	360"	17"
G13	4	5 and 6	55.2"	208.8"

3.2.4 Signal Creation Procedure

On November 16th, 2015, two iGrav gravimeters, and the associated components arrived at the NIST-1 facility at Oregon State University. Dr. Richard Warburton and Mr. Richard Reineman from GWR, Inc., and Dr. Jeff Ridgway from ISL arrived to help with the instrument set up and data collection. Dr. Warburton and Mr. Reineman demonstrated how to set up the meters from their shipping containers. This consisted of the two gravimeters, a baseplate and stabilizing feet for each gravimeter, and various electrical connections necessary to collect data. The each gravimeter was already full of liquid helium, and the spheres were partially suspended. The first meter, designated as G03, was set up in the most stable configuration possible; right next to the CPV on the cement floor of the testing facility. The G03 gravimeter was connected to the controlling laptop by a CAT5 cable to allow the coomputer to monitor and control the instrument. With the software designed specifically for the iGrav system, Dr. Warburton began re-centering the sphere in the gravimeter. The stabilizing of the sphere involved adjustments of the current supplied to the upper and lower superconducting wires, and time to allow the oscillations of the suspended sphere to dissipate. While this was occurring, the other gravimeter, designated as G13, was lifted and then placed on a platform sitting above the top of the CPV. This gravimeter was chosen to be lifted to the top of the CPV because it had a wireless card, allowing us to control the meter without it being hardwired to the computer. A barometer was placed just outside the testing facility, in order to get atmospheric pressure conditions during the entire test. The sphere in the G13 gravimeter was then re-centered and both meters were allowed to settle overnight. During the test, various fill and drain sequences were used in order to create an environment for the gravimeters to capture the change in liquid level in the CPV. There are six events which were captured during this experiment. As stated earlier, one gravimeter, designated as G03, was in the same position throughout all six events. The other gravimeter,

G13, was moved around, to four different locations. The configuration of the gravimeters and the events are described in the following list:

- Event 1: Fill from empty to half full, Fill from half full to full, Drain from full to empty; G13 Position 1
- Event 2: Fill from empty to half full, Fill from half full to full, Drain full to empty; G13 Position 2
- Event 3: Fill from empty to half full, Drain from half full to $1/4$ full, Drain from $1/4$ to empty; G13 Position 2
- Event 4: Fill from empty to $1/4$, Fill from $1/4$ to $1/2$, Drain from $1/2$ to $1/4$, Drain from $1/4$ to $1/8$, Fill from $1/8$ to $1/4$, Drain to empty, Fill from empty to $1/4$, Fill from $1/4$ to $1/2$, Drain from $1/2$ to $1/4$, Drain to empty; G13 Position 3
- Event 5: Fill from empty to half, Fill from half to $3/4$, Fill from $3/4$ to full, Slow Drain to Empty; G13 Position 4
- Event 6: Fill to $1/3$, Fill to $2/3$, Fill to Full, Drain to $2/3$, Drain to $1/3$, Drain to Empty; G13 Position 4

Chapter 4: Results & Discussion

This section presents the results of the the simulations performed using the Matlab script, as well as a comparison of those results to experimental data taken at the NIST-1 facility. First, the characterizations of two vessels at NIST-1 facility, the CNV and CPV, are shown. The results from the cooling pool liquid level measuring experiment are then presented, followed by a comparison between the expected signals given the level in the cooling pool and the actual signals. The data from the gravimeters was manipulated in order to isolate the data of interest to compare with the simulation. A conversion from volts to Gal was applied to each data set using a calibration coefficient from GWR, Inc. The data was then smoothed using a 125 second filter and decimating from 1 second sampling, to 10 second sampling. This removed large non-physical fluctuations which were well outside the ranges of any of the contributions to the signal mentioned in Section 2.2.2. Next, the tidal (both earth and oceanic) noise was simulated and subtracted from the data. Each of the six events were then isolated according to the fill/drain event schedule in Section 3.2.4. Next, the root mean square (RMS) of each "zero" signal data set from each event was removed from the data. This allowed the magnitudes of the simulation and the data to be compared directly, and show any residual distortions not filtered from the data. A discussion of the results then concludes this chapter.

4.1 Simulation

The NIST-1 facility was analyzed before the gravimeter experiment started using the simulation described in Section 3.1. This gave an idea of the possible signals which would be seen by the iGravTM systems. Two vessels were looked at, the CNV and CPV, since the RPV is much smaller in terms of volume and therefore

not expected to produce a usable signal magnitude. Section 3.1 describes how the vessels were characterized, with the minimum number of points in each direction (z , r , and θ). The simulated maximum observable signal for each vessel is listed in Table 4.1. With the minimum number of points along each axis as defined by Section 3.1, the NIST-1 CNV and CPV were simulated to give their theoretical maximum signal.

Table 4.1: Simulation of NIST-1 Vessel Signals

Vessel	z points	r points	θ points	Max Signal (μGal)
CNV	28	62	22	2.3
CPV	28	62	22	5.6

The location of the largest signal on the CNV was at the top of the second cylinder (5.1 m), at the outer radius of the second cylinder (0.386 m). The location of the maximum signal seen by the CPV was at the top or bottom of the pool. In either case the signal magnitude is the same, but the sign is flipped since the gravitational acceleration experienced by the sphere while on top of the CPV is in the positive (downward) direction, and negative (upward) when at the bottom of the CPV. These results showed that the CPV was expected to give a maximum signal magnitude approximately twice as large as one given by the CNV. Both vessels were characterized to standard temperature and pressure to show a maximum signal. This is a good assumption for the CPV, since it will mostly contain standard temperature and atmospheric water during normal operation. The CNV, however, will most likely be operated while filled with superheated steam, therefore lowering the average density of the fluid in the vessel compared to the simulation of the maximum signal. For these two reasons, the CPV was chosen to be characterized by the iGrav systems.

4.2 CPV Characterization Experiment

Two iGrav gravimeters were rented to Oregon State University by GWR, Inc. from November 16th through November 20th, 2015. During that time, as stated earlier, the gravimeters were placed in various locations around the CPV in order to show how well the gravimeters can characterize the vessel. The CPV was filled and drained multiple times, as seen in Figure 4.1. The CPV level was captured using a Rosemount differential pressure meter designated as LDP-6001. This data, in addition to the gravimeter location data in Table 3.1, is used to simulation the expected signal.

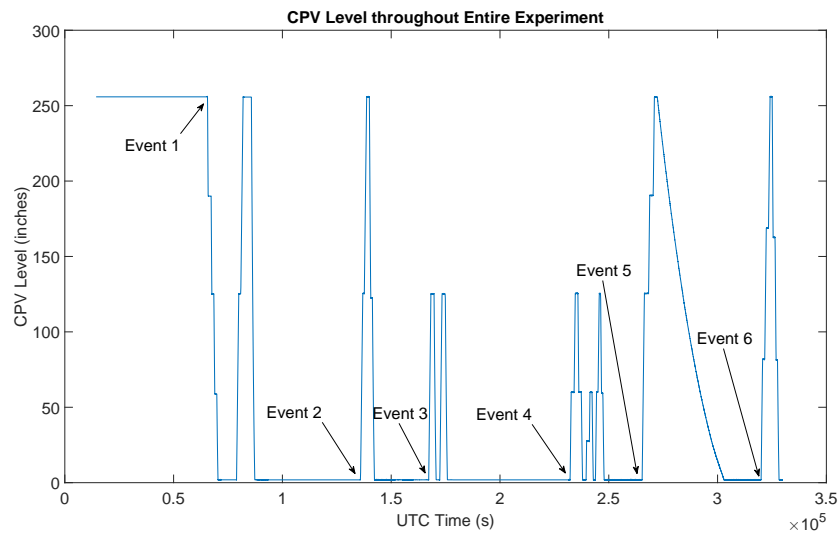


Figure 4.1: CPV Water Level Throughout Entire Experiment

4.3 Raw Data

The raw data from the experiment is presented below. This raw data has already had the voltage-to- μGal conversion constants applied. According to Dr. Richard Warburton of GWR, Inc., the calibration constant for the G03 gravimeter, is 940.0

$(\text{nm}/\text{s}^2)/\text{volt}$, and $880.6 (\text{nm}/\text{s}^2)/\text{volt}$ for the G13 gravimeter [5]. The following plots show each of the gravimeters raw signals over the entire experiment, with each event from Section 3.2.4 labeled.

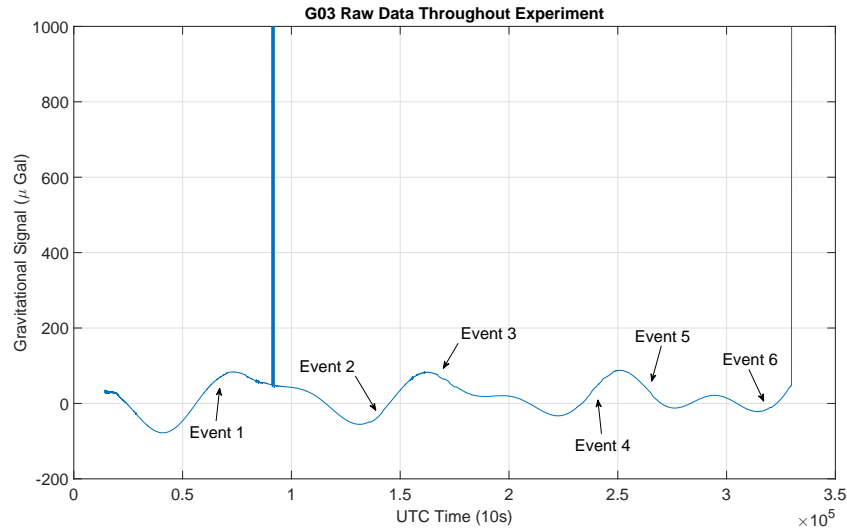


Figure 4.2: G03 Gravimeter Raw Signal Throughout Entire Experiment

There are a couple of things to note from this data. First, in Figure 4.2, there are clearly two abnormally large spikes in the data, one at approximately 0.8×10^5 seconds, and the other at the last data point. The first is due to a loss of signal between the gravimeter and the data collection computer. The second large spike is due to the gravimeter being disconnected from the data collection computer during disassembly of the gravimeter configuration at the end of the experiment. As explained in the following sections, both of these signals are clearly not realistic data, and fall out of the trends when the filtering algorithms are applied. Since this meter was set up before the G13 meter, the dampening of the suspended sphere is mostly complete when data collection was started. A small portion of the beginning data points show the final decay of the oscillating sphere, and is much more prominent in the G13 raw signal in Figure 4.2.

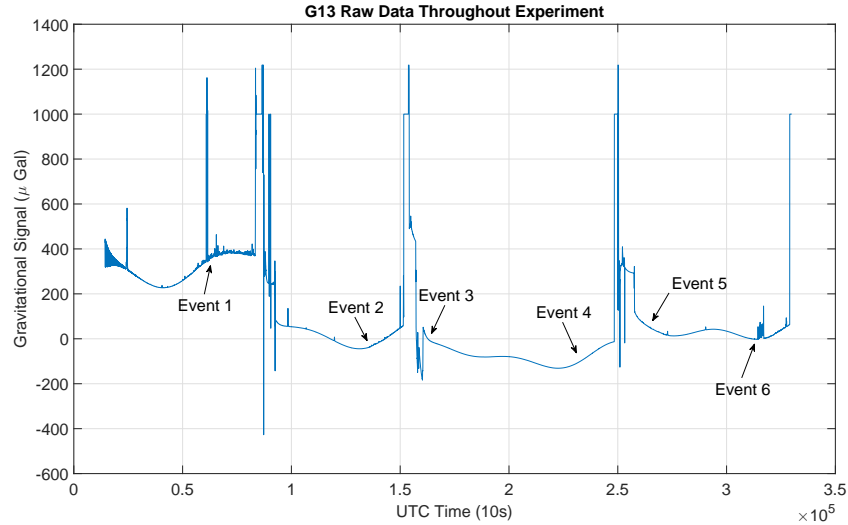


Figure 4.3: G13 Gravimeter Raw Signal Throughout Entire Experiment

Figure 4.3 shows the data from the G13 gravimeter after the calibration constant was applied. Right away, one can tell that this meter was much noisier than the G03 gravimeter, as there are many more sharp spikes in the data. The changes in location of the instrument can clearly be seen as large discontinuous jumps in the signal. There are more of the same loss of signal throughout the experiment, as was seen with the G03 gravimeter. Again, after applying the filtering algorithms, and specifically look at each event individually, much of the extreme spikes are lost. Looking at the earliest data points, the leveling out and calming down of the suspended sphere can be seen as a decaying oscillatory behavior. This continued for around 0.125×10^5 seconds (~ 3.5 hours), and the meter was left untouched throughout the first night until the first event.

Overall, the maximum change in magnitude between peaks and troughs shown in both figures is on the order of $100 \mu\text{gal}$. As described in Section 2.2.2, most of the signal seen in this raw data, results from the environmental noise, including solid earth and oceanic tides. The following sections will show how the noise is filtered out, and will look at each event individually.

4.4 Tide Removal

The largest contribution to noise in the gravimeter signals comes from the oceanic and earth tides. The largest variations in the gravimeter signals from tidal noise are typically around $300 \mu\text{gal}$ peak to trough at mid-latitude locations, with many different factors contributing to the signal. [23][43]

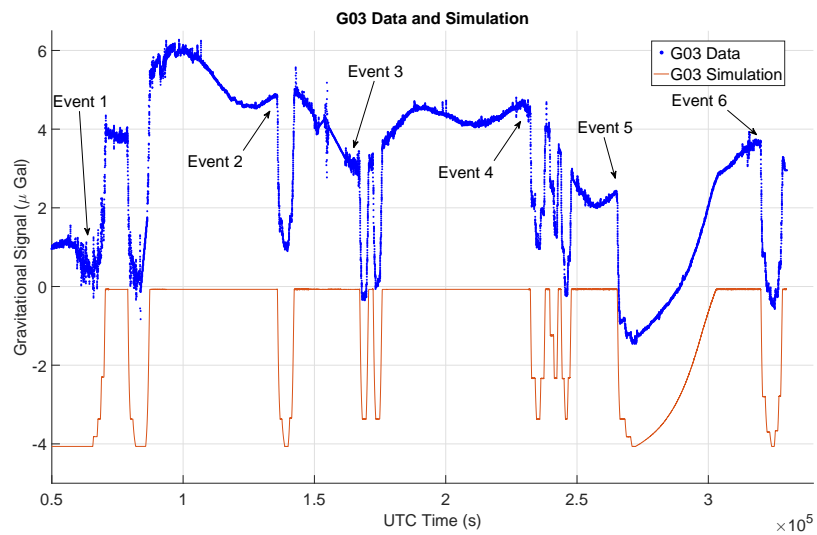


Figure 4.4: G03 Data with Tides Subtracted, and Simulation Throughout Experiment

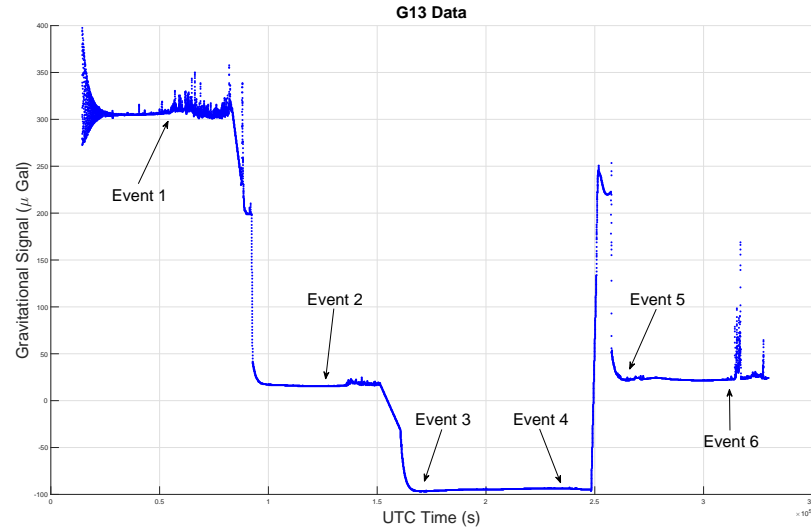


Figure 4.5: G13 Data with Tides Subtracted, and Simulation Throughout Experiment

The above figures (4.4 and 4.5) show the entire experiment with all six events labeled, after the tides and environmental noise due to humidity and moisture effects have been removed. Figure 4.4 shows the impact of filtering out the majority of the noise due to tidal effects and humidity and moisture effects on the G03 gravimeter. It can also be seen that the maximum change in magnitude due to an event is very similar to the predicted value of the simulation, around $4 \mu\text{gal}$. There is, however, residual noise which was not captured from the filtering process. It is difficult to completely filter out the remaining tides without significant background data being taken. The experimental signal is also not calibrated for a specific range in the above figures. This results in the large discrepancies between the simulation and the experimental data from the G03 gravimeter. Therefore, each individual event will be looked at and compared to the corresponding simulated event in the following section.

The plot for the G13 gravimeter, Figure 4.5, is more clear than the raw data, but still shows the extreme changes in signal due to the gravimeter moving throughout the different testing locations. Because the magnitude of these changes is on the order of a few hundred μgal , the individual events are "washed out" in this figure. There are two reasons the simulation for the G13 gravimeter is not shown in this figure. First, the gravimeter was moved often enough to not have a consistent location relative to the CPV. The other reason is that the magnitude of the raw signal from the gravimeter is much larger than the simulation magnitudes. In order to compare the simulation and experimental data, the RMS of the "zero signal" must be subtracted from the individual event data set. This is shown in the following section.

4.5 Comparison

In this section, each of the data sets from the individual gravimeters will be broken in to the time section where each event occurred. The data is then compared to a simulation of the theoretical signal using the level information gathered from LDP-6001. For each of the simulations, as stated earlier, the CPV was assumed to be perfectly cylindrical, and the fluid was assumed to be at $\sim 55^\circ\text{F}$. The experimental data was moved to a different location based on the signal from the simulation while the level in the CPV was at a minimum. For example, the signal seen for event 2 by gravimeter G03 in Figure 4.11, starts at approximately $5 \mu\text{gal}$, even though the CPV level was at a minimum. The entire data set for this event was brought down such that the data starts at $0.1 \mu\text{Gal}$, corresponding to the average simulated signal while the CPV level was at a minimum. This allows a direct comparison between the experimental data and the simulated signal on a per event basis. Each of the events were isolated from the overall data set, and then their zero signal RMS was calculated. As can be seen in most of the following figures, there is some variation between the simulation and the experimental data which progresses throughout the event, making the two become further and further off. This will be touched

on more in the next section, but is likely due to a number of factors, including incomplete tide removal, and deflection in the facility flooring. Event 4 is specially investigated, once by following the same method as other events, and the other because the G13 gravimeter data was subtracted from the G03 signal during this event.

4.5.1 G03 Gravimeter

This section presents the individual event results from the G03 gravimeter. This experimental data has been filtered of oceanic and solid earth tides as described in Section 2.2.3. This instrument did not move during the entire experiment, and therefore produced the least noisy data out of the two gravimeters. The data from this meter is compared to the signal calculated by the simulation, and the CPV level recorded by LDP-6001. The RMS signal of the experimental data during each period of the event where LDP-6001 read a minimum signal is calculated, then subtracted from the entire events data set. These RMS values are presented in Table 4.2. During the periods where the level is not changing, the RMS and standard deviation of both the experimental data and the simulated signal are calculated. These results are presented in Table 4.3.

Table 4.2: Zero RMS Signals for G03

Event	RMS Signal (μGal)
1	3.8388
2	4.8866
3	3.2811
4	3.7205
5	2.6341
6	3.3976

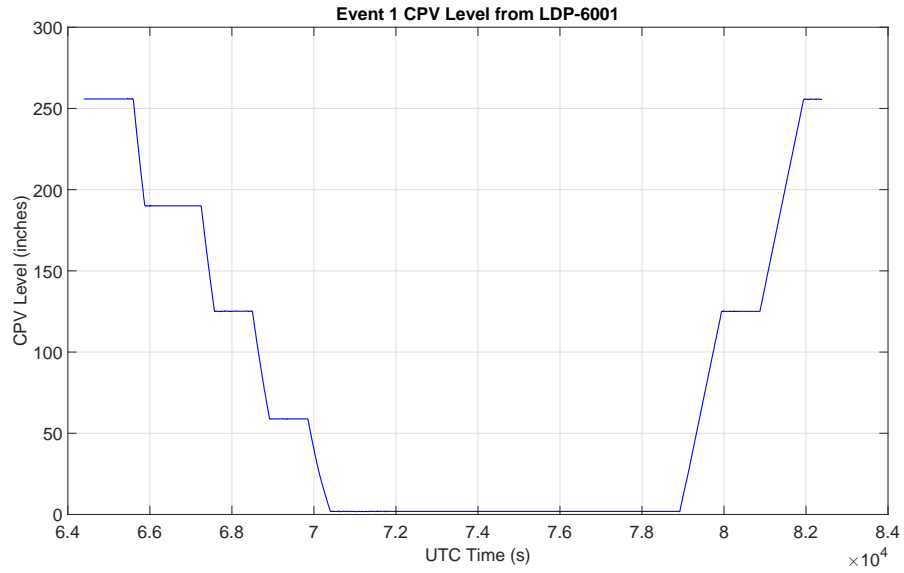


Figure 4.6: Event 1 CPV Level from LDP-6001

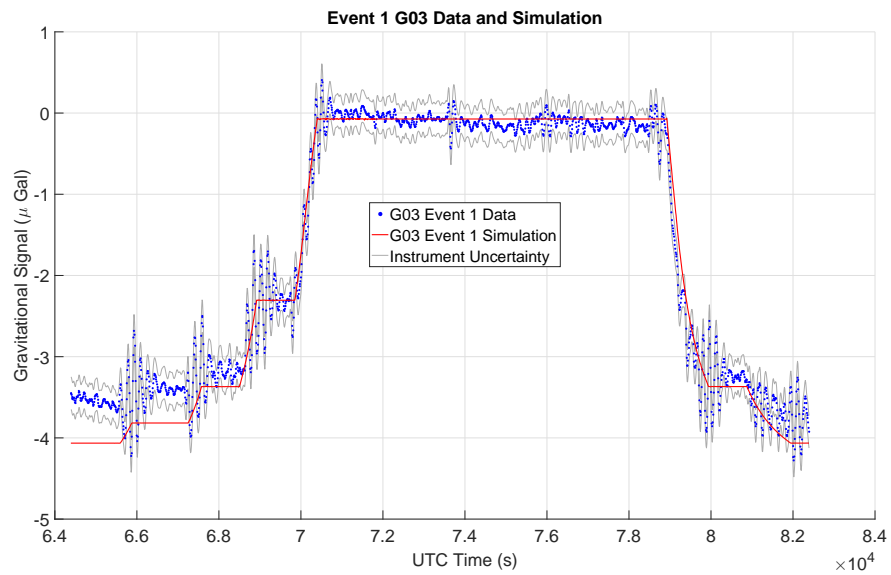


Figure 4.7: Event 1 G03 Gravimeter Signal and Simulation

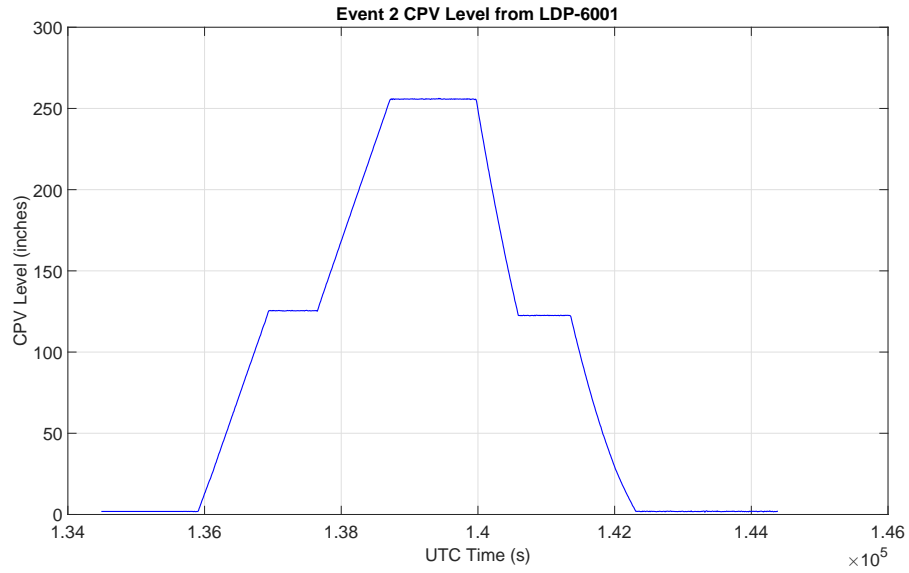


Figure 4.8: Event 2 CPV Level from LDP-6001

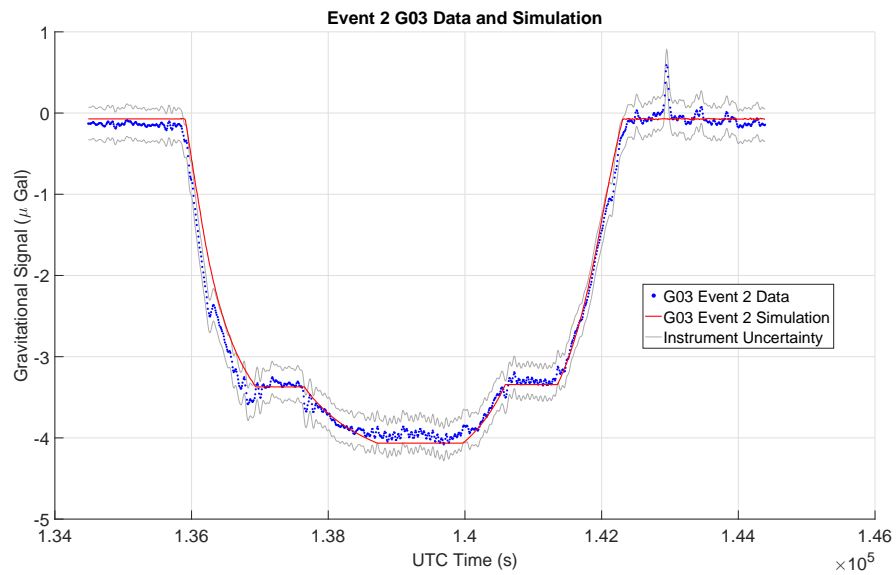


Figure 4.9: Event 2 G03 Gravimeter Signal and Simulation

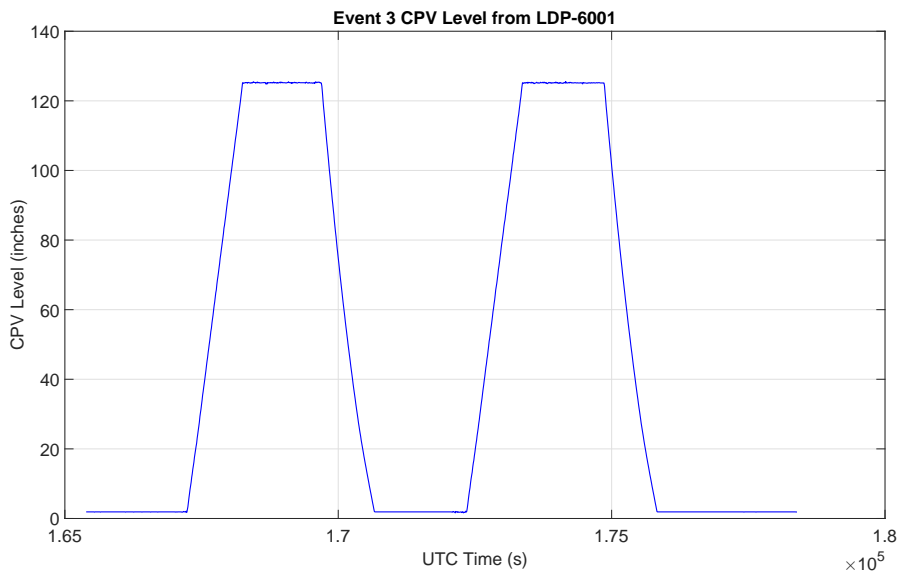


Figure 4.10: Event 3 CPV Level from LDP-6001

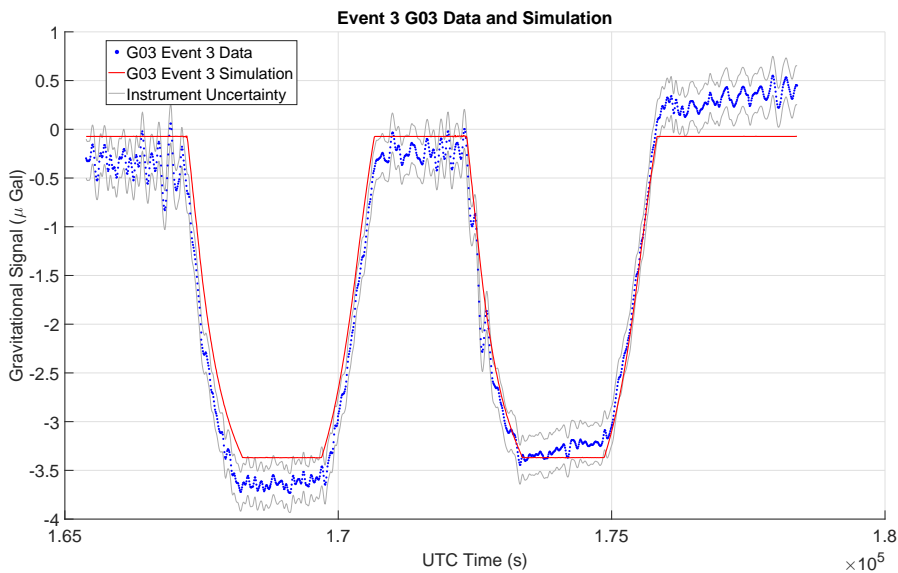


Figure 4.11: Event 3 G03 Gravimeter Signal and Simulation

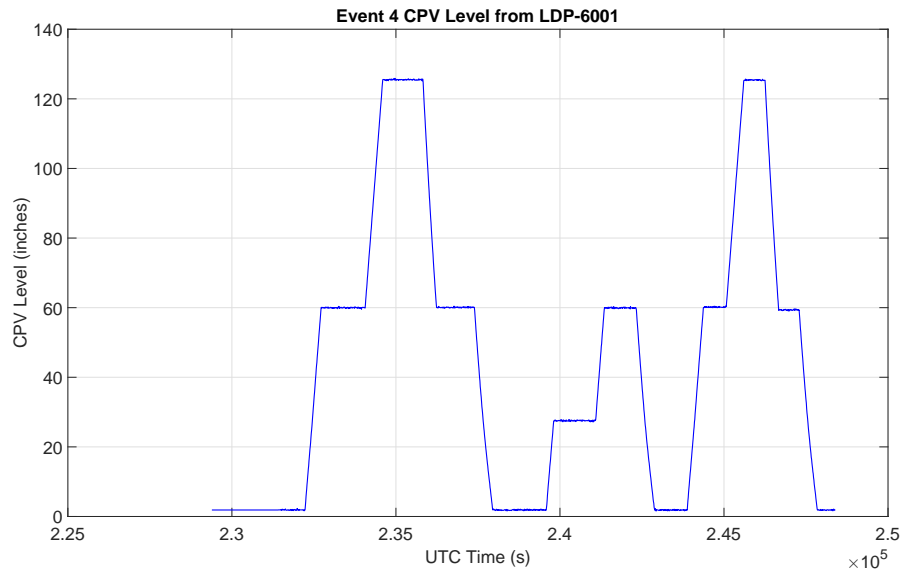


Figure 4.12: Event 4 CPV Level from LDP-6001

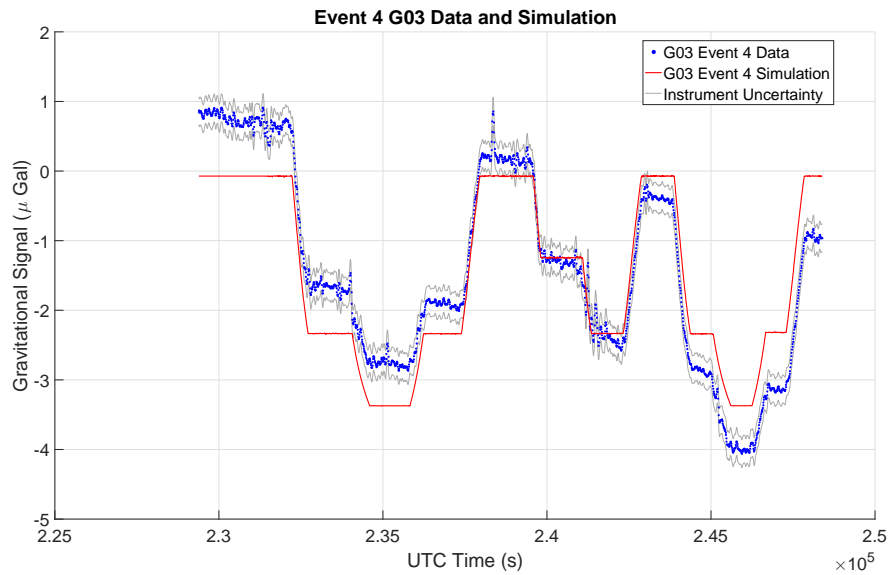


Figure 4.13: Event 4 G03 Gravimeter Signal and Simulation

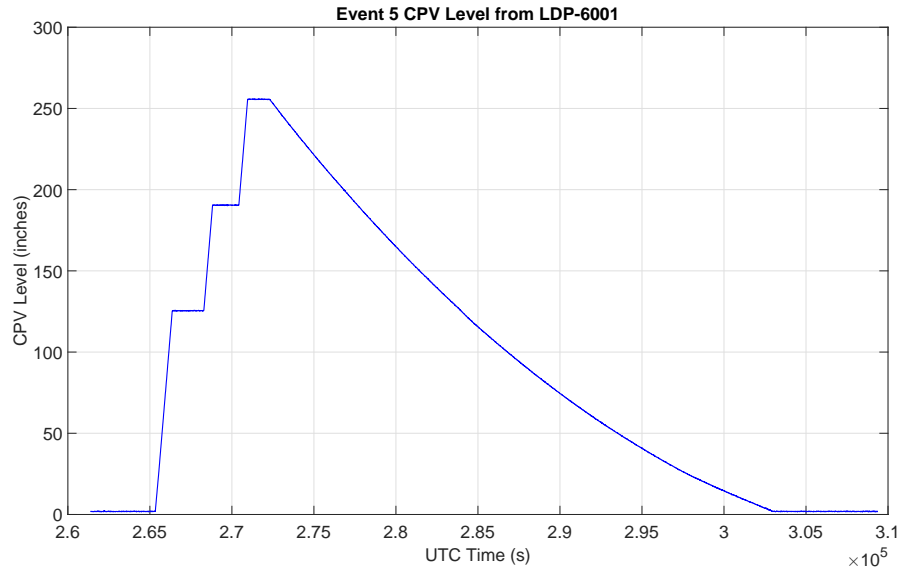


Figure 4.14: Event 5 CPV Level from LDP-6001

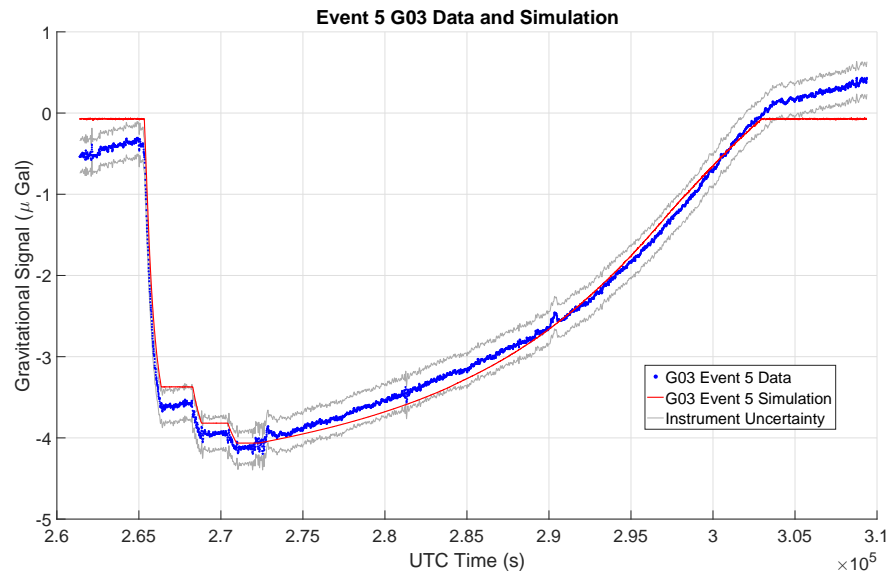


Figure 4.15: Event 5 G03 Gravimeter Signal and Simulation

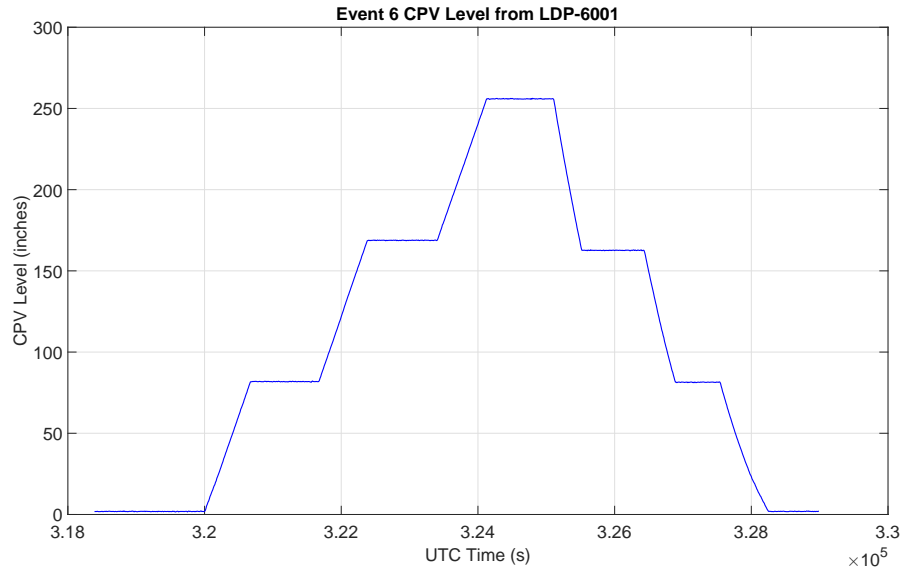


Figure 4.16: Event 6 CPV Level from LDP-6001

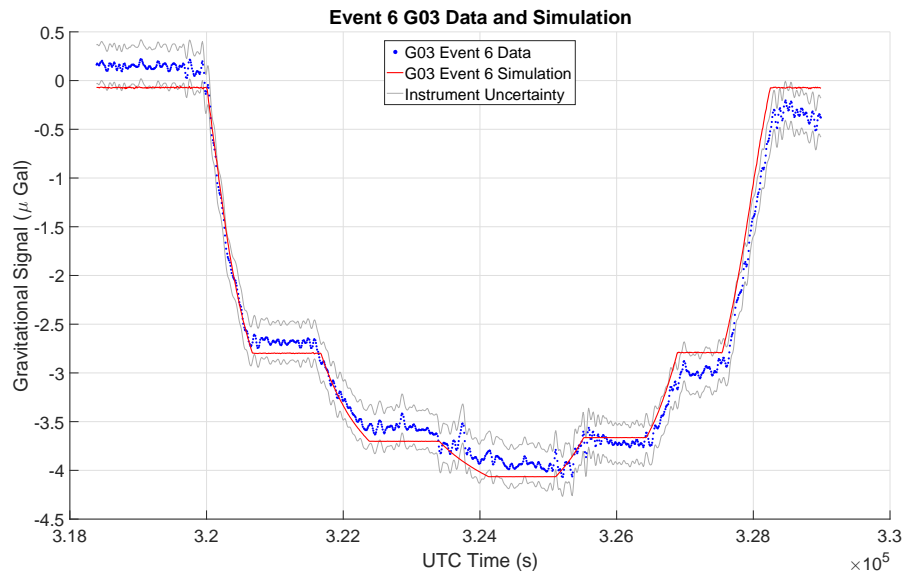


Figure 4.17: Event 6 G03 Gravimeter Signal and Simulation

The following table shows the results from the G03 gravimeter throughout the entire experiment. Each event is labeled by number, and the periods of time between each event is labeled as "N/A". During each constant level, the time averaged CPV Level recorded by LDP-6001 is shown in inches of water. Next, the RMS of both the experimental data and the simulation is calculated and presented in μGal . This indicates how well the magnitude of the filtered signal corresponds to the simulated signal. Finally, the standard deviation σ for both the experimental data and the simulation is calculated and presented in μGal . This shows how stable the signal was during the constant level period.

Table 4.3: G03 Results for Entire Experiment

Event	CPV Level_{Avg}	RMS_{Data}	RMS_{Sim}	σ_{Data}	σ_{Sim}
1	255.8 in	3.4468	4.0647	0.0602	0.00014
	190.0	3.2934	3.8167	0.2017	0.00025
	125.1	3.0758	3.3688	0.1851	0.00097
	58.8	2.2394	2.3052	0.2861	0.00145
	1.9	0.1015	0.0732	0.1015	0.00168
	125.1	3.1337	3.3681	0.1613	0.00059
	255.7	3.6745	4.0642	0.2832	0.00029
2	1.9	0.0468	0.0722	0.0234	0.00041
	125.5	3.2469	3.3720	0.0473	0.00098
	255.8	3.8747	4.0645	0.0467	0.00036
	122.5	3.2018	3.3432	0.0335	0.00100
	1.9	0.1182	0.0730	0.1118	0.00510
3	1.9	0.2954	0.0732	0.1593	0.00085
	125.2	3.5258	3.3696	0.0512	0.00099
	1.9	0.1638	0.0730	0.0905	0.00177
	125.2	3.1883	3.3692	0.0628	0.00092
	1.9	0.4241	0.0733	0.0942	0.00028

Event	CPV Level_{Avg}	RMS_{Data}	RMS_{Sim}	σ_{Data}	σ_{Sim}
4	1.9	0.8290	0.0724	0.1085	0.00216
	60.0	1.5786	2.3345	0.0623	0.00320
	125.5	2.6580	3.3724	0.0710	0.00116
	60.1	1.8082	2.3368	0.0430	0.00281
	1.9	0.3306	0.0724	0.1348	0.00456
	27.5	1.2006	1.2441	0.0731	0.00560
	59.9	2.2747	2.3333	0.1439	0.00334
	1.9	0.2870	0.0719	0.0529	0.00420
	60.1	2.7676	2.3387	0.0450	0.00280
	125.4	3.9008	3.3716	0.0394	0.00093
	59.3	3.0398	2.3183	0.0415	0.00310
	1.9	0.8475	0.0721	0.0478	0.00393
5	1.9	0.3403	0.0721	0.0682	0.00460
	125.4	3.4978	3.3719	0.0259	0.00109
	190.4	3.8484	3.8187	0.0199	0.00054
	255.6	4.0123	4.0641	0.0375	0.00031
Slow Drain	105.0	2.7325	2.8873	1.1439	1.20284
	1.9	0.3465	0.0726	0.1042	0.00467
6	1.9	0.2464	0.0721	0.0360	0.00428
	81.8	2.5811	2.7984	0.0288	0.00214
	168.8	3.4579	3.7018	0.0427	0.00065
	255.9	3.8364	4.0649	0.0414	0.00038
	162.6	3.6030	3.6639	0.0417	0.00079
	81.4	2.8917	2.7912	0.0545	0.00205
	1.9	0.2542	0.0733	0.0692	0.00405

4.5.2 G13 Gravimeter

This section presents the data from the individual events as seen by the G13 gravimeter. As was done with the G03 gravimeter data, the plots show a comparison between the experimental data, the simulated signal, and the CPV level recorded by LDP-6001. Where the level in the CPV was at a minimum per LDP-6001, the RMS of the experimental data was calculated and then subtracted from the entire event data set. These values are presented in Table 4.4. During the periods where the level in the CPV is constant, the RMS and standard deviation of the experimental data and the simulated signal are calculated and presented in Table 4.5.

Table 4.4: Zero RMS Signals for G13

Event	RMS Signal (μGal)
1	305.6829
2	16.6581
3	96.0952
4	94.2219
5	21.9616
6	23.9235

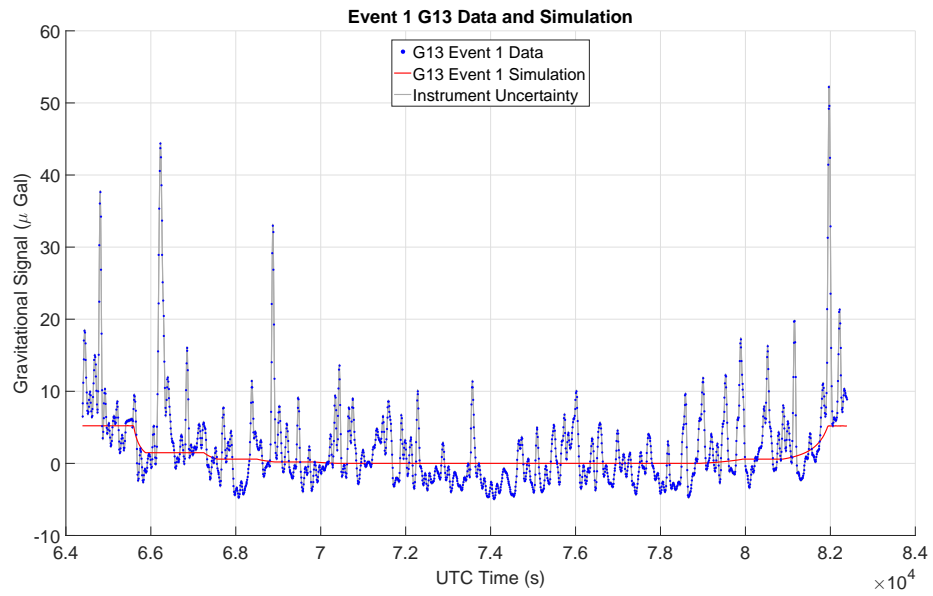


Figure 4.18: Event 1 G13 Gravimeter Signal and Simulation

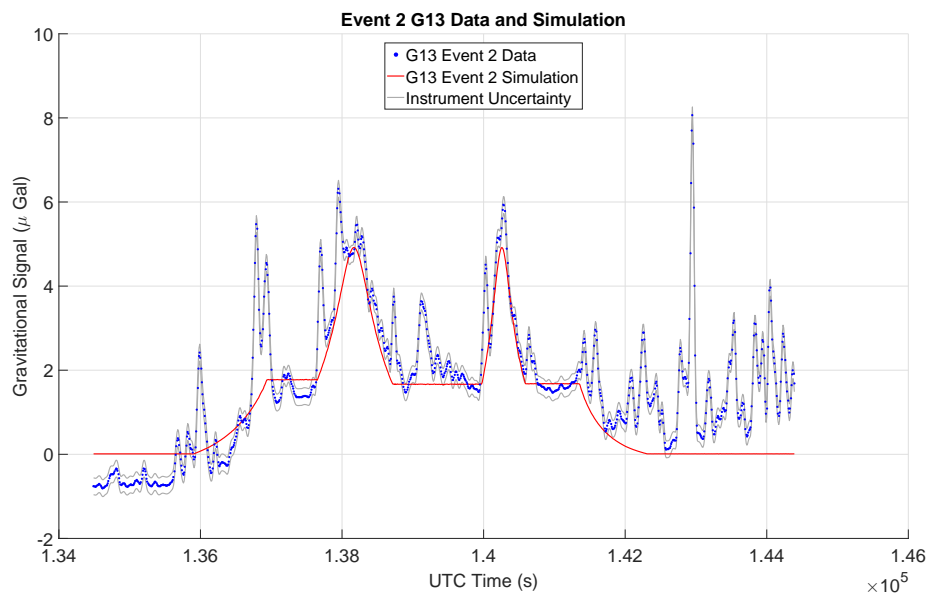


Figure 4.19: Event 2 G13 Gravimeter Signal and Simulation

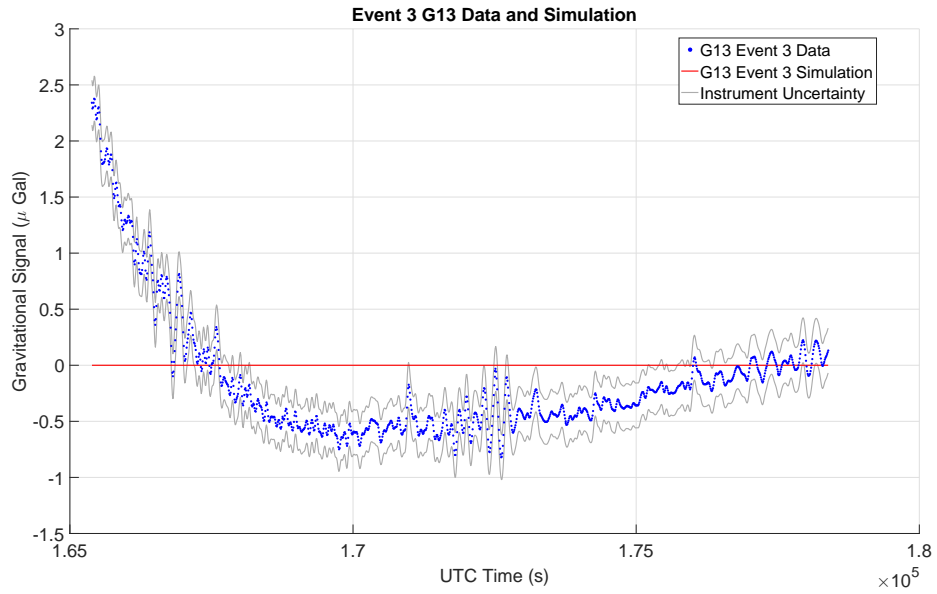


Figure 4.20: Event 3 G13 Gravimeter Signal and Simulation

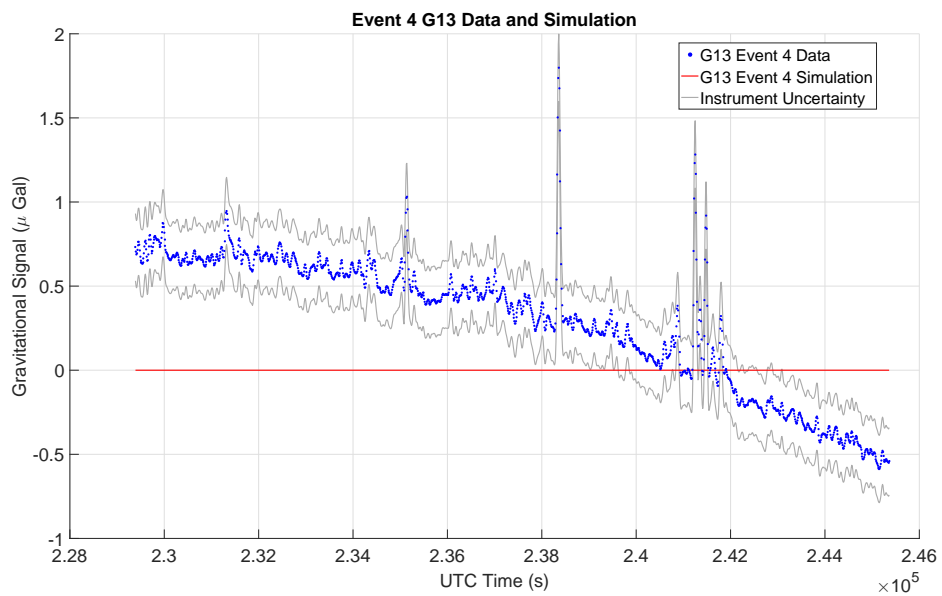


Figure 4.21: Event 4 G13 Gravimeter Signal and Simulation

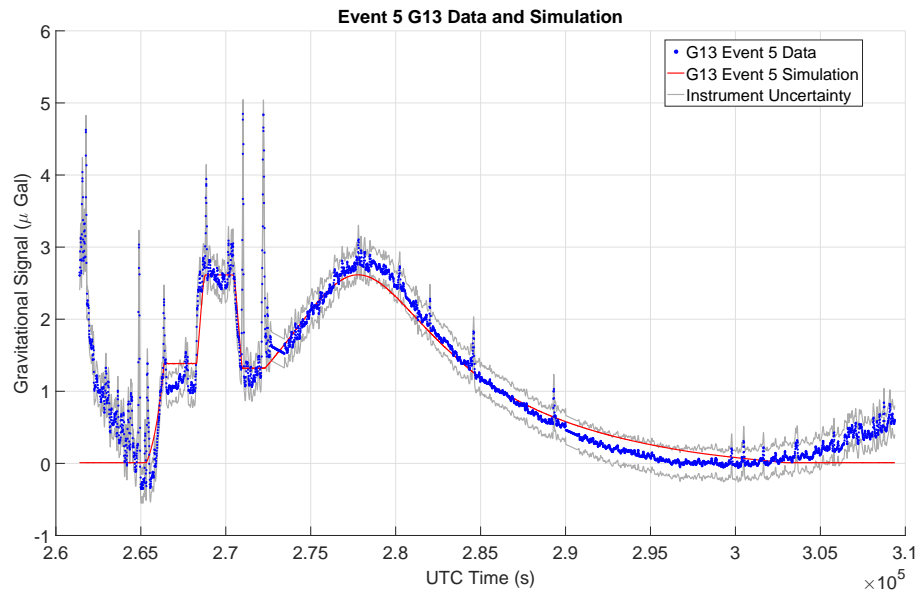


Figure 4.22: Event 5 G13 Gravimeter Signal and Simulation

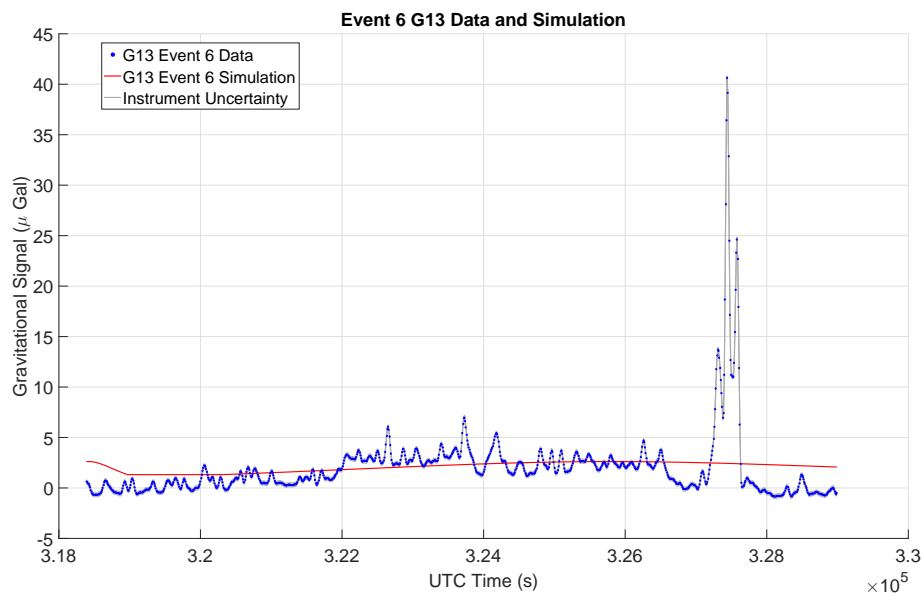


Figure 4.23: Event 6 G13 Gravimeter Signal and Simulation

As was done with the G03 data, the G13 data is presented in tabular format below. Each event is numbered, but the data between each event is not considered with this meter, since it was moved often throughout the experiment. The time averaged CPV Level as recorded by LDP-6001 is presented next. This is followed by the experimental and simulation RMS and standard deviations.

Table 4.5: G13 Results for Entire Experiment

Event	CPV Level_{Avg}	RMS_{Data}	RMS_{Sim}	σ_{Data}	σ_{Sim}
1	255.8	10.7242	0.5215	6.5796	0.0661
	190.0	11.7360	0.1480	9.7401	0.0114
	125.1	4.1410	0.0590	4.1390	0.0083
	58.8	3.3930	0.0197	3.2924	0.0024
	1.9	3.2885	0.0005	3.2904	0.0011
	125.1	4.9792	0.0589	4.2535	0.0005
	255.7	19.8001	0.5193	13.0118	0.0014
2	1.9	2.2612	0.0011	0.2422	0.0001
	125.5	0.2725	0.1774	0.2435	0.0034
	255.8	0.6903	0.1666	0.5343	0.0037
	122.5	0.1741	0.1678	0.1754	0.0032
	1.9	1.2634	0.0011	1.2651	0.0007
3	1.9	1.0929	0.0011	0.6300	0.0001
	125.2	0.6790	0.1765	0.0759	0.0034
	1.9	0.7021	0.0011	0.1093	0.0002
	125.2	0.5762	0.1764	0.0651	0.0032
	1.9	0.2224	0.0011	0.1056	0.0000

Event	CPV Level_{Avg}	RMS_{Data}	RMS_{Sim}	σ_{Data}	σ_{Sim}
4	1.9	0.7182	0.0001	0.0618	0.0000
	60.0	0.6169	0.0116	0.0373	0.0000
	125.5	0.5437	0.0396	0.1247	0.0001
	60.1	0.4827	0.0116	0.0523	0.0000
	1.9	0.4542	0.0001	0.2739	0.0000
	27.5	0.1485	0.0034	0.0762	0.0000
	59.9	0.2345	0.0115	0.2311	0.0000
	1.9	0.2739	0.0001	0.0461	0.0000
	60.1	0.4273	0.0116	0.0448	0.0000
	125.4	0.6390	0.0395	0.0532	0.0001
	59.3	0.7240	0.0114	0.0387	0.0000
	1.9	0.8324	0.0001	0.2324	0.0000
5	1.9	1.5326	0.0000	0.9955	0.0000
	125.4	1.2708	0.0015	0.1627	0.0000
	190.4	2.7551	0.0029	0.1498	0.0000
	255.6	2.1020	0.0014	1.0338	0.0000
Slow Drain	105.0	1.5296	0.0015	0.9782	0.0010
	1.9	0.4692	0.0000	0.1830	0.0000
6	1.9	0.4920	0.0010	0.4746	0.0006
	81.8	1.0473	0.0686	0.4724	0.0016
	168.8	3.3848	3.7018	0.0425	0.0007
	255.9	2.6135	0.1376	0.9182	0.0029
	162.6	2.6610	0.2451	0.6209	0.0033
	81.4	0.6024	0.0681	0.3711	0.0015
	1.9	0.5324	0.0010	0.5174	0.0005

4.6 Signal Subtraction

The next method used to characterize the CPV is the subtraction of the signal from the G13 gravimeter from the signal from the G03 gravimeter. This was done to attempt to cancel out large environmental signals seen by both gravimeters, and to increase the maximum magnitude of the signals seen by the gravimeters. The following plots show the resulting signal, with no subtraction of simulated environmental signals. It is clear that the signal from the gravimeters is more stable and closer to the simulated value using this method.

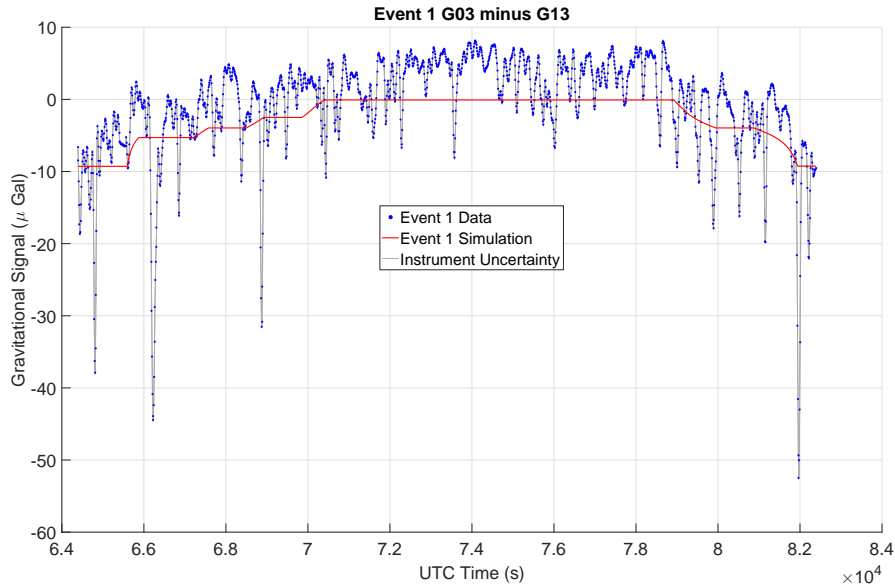


Figure 4.24: Event 1 Subtraction Signal and Simulation

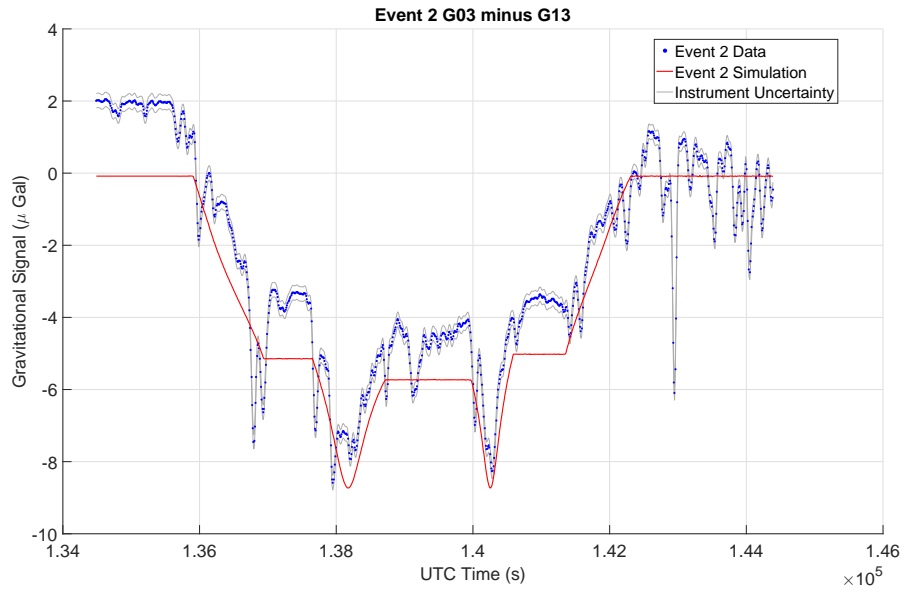


Figure 4.25: Event 2 Subtraction Signal and Simulation

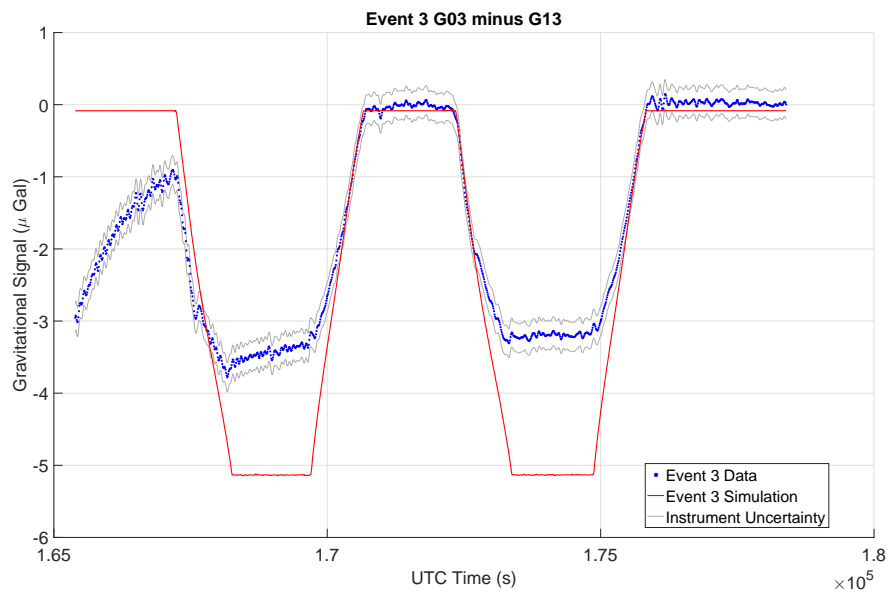


Figure 4.26: Event 3 Subtraction Signal and Simulation

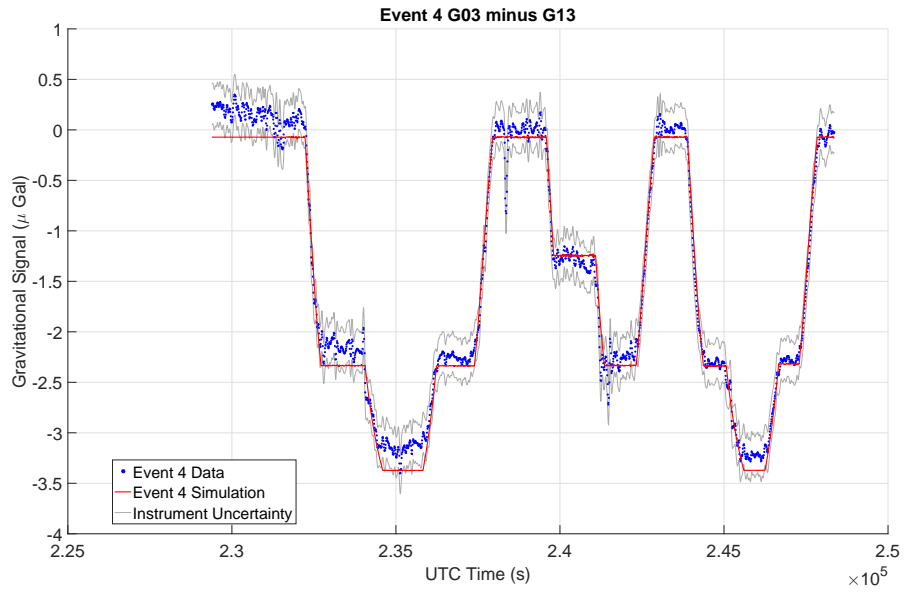


Figure 4.27: Event 4 Subtraction Signal and Simulation

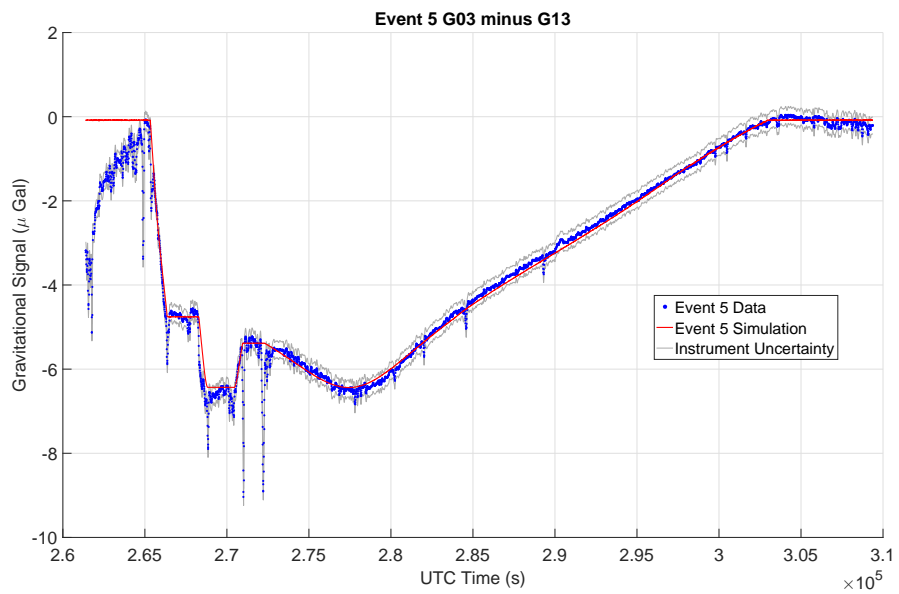


Figure 4.28: Event 5 Subtraction Signal and Simulation

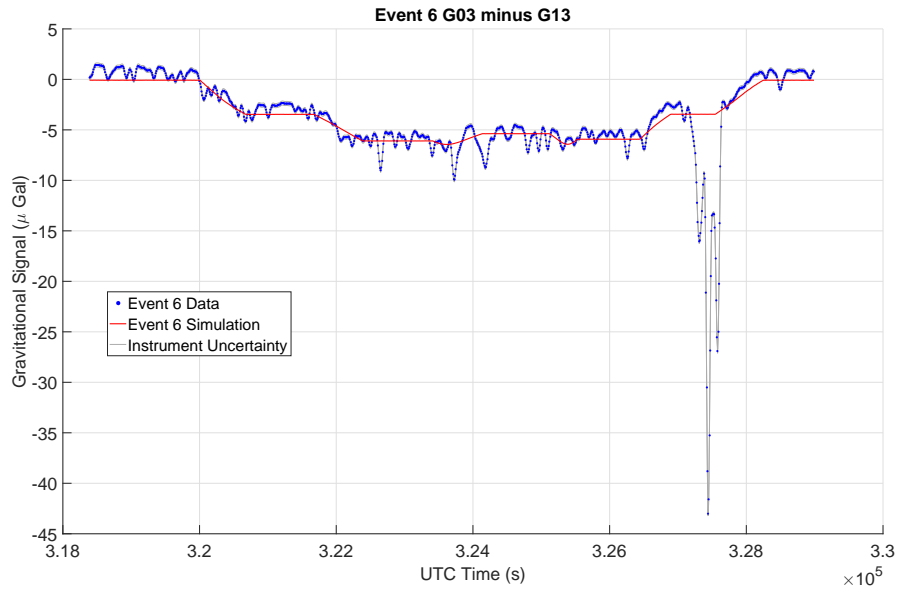


Figure 4.29: Event 6 Subtraction Signal and Simulation

4.7 Discussion

After the signal from the gravimeters is converted from Volts to μGal , it is not very clear where each individual event occurs. The signal is drowned out by multiple noise signals captured by the gravimeters. It is clear however, that there is a period during the set-up of the gravimeter where the signal oscillates rapidly. This signal calms down over a few hours, as the levitated sphere comes to rest. This contribution to the signal can be seen in Event 1 on both the G03 and G13 gravimeters. While the G03 gravimeter signal is fairly stable, there are still some large oscillations, especially when the CPV is drained or filled. The G13 gravimeter clearly did not have enough time to settle, and the platform it rested on was not stable enough. Any and all vibrations around the CPV were magnified and captured as large spikes in the gravimeter. This also had an impact on the data for Event 3, as the event occurred relatively soon after the second move of the G13 gravimeter. After attempting to perform the same subtraction of G13 signal from the G03 signal, it is clear that the G13 sphere was not given enough time to settle. This can be seen as a decaying signal at the beginning of the event. The data for Event 3 from G13 is therefore unusable. If gravimeters were to be used to measure liquid inventory in a nuclear power plant environment, a settling period of approximately 1 day is required for the signal to be reliable after any movement of the meters.

The most important step in processing the data is subtracting the contribution of the tides from the signal. The method which is commonly used to look at single gravimeter data shows that a simulated tidal impact can be subtracted from the data to produce any local affects. All of the data from the G03 gravimeter easily shows the individual events and the steady periods of no level change in the CPV. There are some remaining tides, which are clearly visible in Figures 4.11, 4.13, and 4.15, as the data is slightly misaligned from the simulation. The other method investigated in this study was to subtract the signals from two gravimeters. This was done to subtract any common noise affects from both signals, and to produce

a larger magnitude signal. Figure 4.27 shows the tides seen by both gravimeters being subtracted out once the signal from G13 is subtracted from G03. This event more closely matches the simulation than the single gravimeter data in Figure 4.13. Figure 4.28 shows that once the signal from G13 is subtracted from G03, the maximum magnitude in the signal increases from approximately $4 \mu\text{Gal}$ to approximately $6.5 \mu\text{Gal}$. One additional impact of the subtraction of the two signals is that any local vibrational noise seen in one meter is not subtracted out and is carried through the data. In this study, the G13 gravimeter was almost always noisier than the G03 gravimeter. This produced generally noisier data during steady level situations once the two signals were subtracted, compared to the single stationary gravimeter signal.

In the data from the individual gravimeters, there are a few relatively large spikes that remain in after the tides have been removed. In event 2, both gravimeters record a spike at approximately 1.4288×10^5 seconds, during a period where the CPV is completely empty and both gravimeters should be reading zero signal. The maximum magnitude of the spike recorded by the G03 gravimeter is approximately $0.6 \mu\text{Gal}$. This spike interrupts a set of data that is otherwise fairly stable. The next largest spike has a trough to peak magnitude of approximately $0.19 \mu\text{Gal}$. The maximum magnitude of the spike recorded by the G13 gravimeter is approximately $8 \mu\text{Gal}$. While this data is more unstable, the next largest spike has a trough to peak magnitude of approximately $3 \mu\text{Gal}$. Since both meters record this unusual spike for the same amount of time, it is likely that a vibration inducing event, such as personnel climbing the facility scaffolding, was the source of the noise. Event 4 also has a couple of spikes which are shared between both gravimeters that clearly stand out compared to the surrounding data. These spikes are not large enough to be non-physical, but still significantly abnormal compared to the surrounding data.

Chapter 5: Conclusion

5.1 Summary

The main objective for this study was to assess the use of the iGrav superconducting gravimeter system to measure liquid inventory in small modular reactors. A simulation was created to calculate the signal seen by the gravimeters placed outside a vessel of interest. The method utilized in the simulation is a differential volumes method, where the volume of interest is broken up in to many small volumes. The gravitational acceleration caused by each differential volume on a specified observational point is summed over the volume of interest. The simulation allows the user to characterize the volume under investigation by specifying the height and radius of a cylindrical volume. A study was performed on the simulation to determine the minimum required number of points along each direction of the volume of interest.

To verify the simulation, the gravitational acceleration caused by the NIST-1 CPV filling and draining was characterized using two iGravTM superconducting gravimeter systems from GWR, Inc. One gravimeter was stationary during the entire event to attempt to capture the maximum and most stable signal. The other was moved several times to characterize different locations and to provide a measurement of background gravitational acceleration. The raw data was manipulated to provide a direct comparison between the simulation results and the experimental data. Oceanic and solid Earth tides, and oceanic loading were simulated then subtracted from the data. The six individual events were investigated individually. The results of this study show that in order to utilize superconducting gravimeters to measure liquid level in vessels to the high precision required

by the nuclear industry, the background signal must be accurately simulated or characterized by an additional gravimeter.

5.2 Future Work

One of the most important considerations shown by this study is the need to characterize the background noise that will always be seen by superconducting gravimeters. The oceanic and solid earth tides must be characterized over the course of months to years for each location to generate a database capable of simulating the future tides accurately enough to allow minimal impact to the gravimeters signal. Another undesirable characteristic of the data in this study is the noise from the daily work in an industrial facility. The NIST-1 facility is much smaller and less staffed than a nuclear power plant. With more people and more instrumentation, the vibrations at a nuclear power plant would likely be much larger compared to the NIST-1 facility. The impact of environmental noise ranges from small, rapid and almost unnoticeable spikes to large, up to a few minutes long fluctuations. Further study on the impact of noise on the iGravTM systems in nuclear power plants is required to discern between environmental noise, and changing level signals.

In order to integrate superconducting gravimeters in to the NuScale SMR instrumentation environment, an enclosure or tunnel must be designed to allow the gravimeters to be located as close to the modules as possible. This enclosure must be sealed to keep water from the cooling pool from destroying the meter and electrical system. It must be designed to allow maintenance to be performed and necessary parts of the refrigeration cycle and electrical system to connect to the meter. A study must then be performed on the impact the enclosure would have on the ability of the cooling pool to transfer heat from the containment wall to the environment. A vibration study on how the structure could isolate the meters from vibrations would also need to be performed. One suggestion would be to secure

the iGravTM systems on noise dampening platforms, and place those platforms on lifts to locate the meters exactly where desired. This system would allow for the extraction of the meters from the enclosure to perform maintenance.

All instrumentation at a nuclear site must adhere to certain specifications and standards in order to ensure that the instrument will work as intended. Either the manufacturer and calibration facilities must be certified under accepted quality assurance programs, such as NQA-1, or must undergo commercial grade dedication. These processes add to the overall cost of using superconducting gravimeters to measure liquid level in nuclear power plants.

The simulation must also be more efficient, and quicker to run. Currently, the simulation calculates the expected signal using differential volumes in cylindrical coordinates. This forces the volume being characterized to be shaped similarly to a cylinder. This does not allow for volumes with complex geometries, such as the NuScale SMR to be simulated accurately. Using a differential volume method with the ability to customize the meshing coordinate system would all characterization of different shaped volumes.

Bibliography

- [1] D. T. Ingersoll, Z. J. Houghton, R. Bromm, and C. Desportes. Nuscale small modular reactor for co-generation of electricity and water. *Desalination Journal*, 340:84–93, 2014.
- [2] International Atomic Energy Agency. Iaea-tecdoc-1474: Natural circulation in water cooled nuclear power plants. 2005.
- [3] Emerson Process Management. Rosemount TM 3051s series of instrumentation, May 2016.
- [4] Inc. GWR Instruments. Igrav superconducting gravity meter. "Thmoas Web Solutions. Web. <<http://www.gwrinstruments.com/pdf/igrav-brochure.pdf>>."
- [5] R. Warburton. *Personal Communication*, April 4th, 2016.
- [6] J. Hinderer, D. Crossley, and R. Warburton. *Treatise on Geophysics*, volume 3. Oxford: Elsevier, 2nd edition, 2015.
- [7] K. Mickus. Gravity method: Environmental and engineering applications. *Department of Geosciences, Southwest Missouri State University*, August 24-28, 2014.
- [8] D. Crossley, J. Hinderer, and U. Ricciardi. The measurement of surface gravity. *Reports on Progress in Physics*, 76:1–47, 2013.
- [9] Idaho National Laboratory. Experimental breeder reactor-i.
- [10] U.S. Energy Information Administration. FAQ: How old are u.s. nuclear power plants, and when was the last one built?, Feb. 4, 2016.
- [11] I. William and D. Magwood. Report to congress on small modular nuclear reactors. *U.S. Department of Energy*, 2001.

- [12] D. Ingersoll, Z. Houghton, R. Bromm, C. Desportes, M. McKellar, and R. Boardman. Extending nuclear energy to non-electrical applications. *19th Pacific Basin Nuclear Conference (PBNC 2014)*, August 24-28, 2014.
- [13] Nuclear Regulatory Commission. Regulatory guide 1.151: Instrument sensing lines revision 1. July, 2010.
- [14] Nuclear Regulatory Commission. Nrc information notice 95-20: Failures in rosemount pressure transmitters due to hydrogen permeation into the sensor cell. March, 1995.
- [15] Nuclear Regulatory Commission. Nrc information notice 92-54: Level instrumentation inaccuracies caused by rapid depressurization. July, 1992.
- [16] S. Rishi. *AdMet Paper No. UM 001*, 2012.
- [17] Emerson Process Management. Rosemount 3051s series product data sheet. May 2016.
- [18] Luis Rodés. A differential gravimeter and its applications. *Publications of the Astronomical Society of the Pacific*, 32:27–36, 1920.
- [19] H. Hanada, T. Tsubokawa, S. Takano, and S. Tsuruta. New design of absolute gravimeter for continuous observations. *AIP: Review of Scientific Instruments*, 58:669–673, 1987.
- [20] MicroG-Lacoste. gphonex brochure.
- [21] R. A. Geyer. *Handbook of Geophysical Exploration at Sea*. CRC Press, 2000 Corporate Blvd., N.W., Boca Raton, Florida 33431, 2nd edition, 1992.
- [22] W. A. Prothero and J. M. Goodkind. A superconducting gravimeter. *The Review of Scientific Instruments*, 39(9):1257–1262, September, 1968.
- [23] J. M. Goodkind. The superconducting gravimeter. *American Institute of Physics: Review of Scientific Instruments*, 70(11):4131–4152, 1999.
- [24] V. R. Karasik and I. Yu. Shebalin. Superconducting properties of pure niobium. *Soviet Physics JETP*, 30(6):1068–1075, June, 1970.
- [25] M. Freybourger, J. Hinderer, and J. Trampert. Comparative study of superconducting gravimeters and broadband seismometers sts-1/z in seismic and

- subseismic frequency bands. *Physics of the Earth and Planetary Interiors*, 101:203–217, 1997.
- [26] R. J. Donnelly and C. F. Barengi. The observed properties of liquid helium at the saturated vapor pressure. *University of Oregon*, 2004.
- [27] L. R. Lawrence. High temperature superconductivity: The product and their benefits. *Oak Ridge National Laboratory*, July 1998.
- [28] D. McChesney. *Brookhaven National Lab, Cryogenic Facility*, 2005.
- [29] R.J. Warburton, H. Pillai, and R.C. Reineman. *Initial Results with the New GWR iGravTM Superconducting Gravity Meter*. International Association of Geodesy (IAG) Symposium Proceedings, St. Petersburg, Russia, June 2010.
- [30] J. Hinderer J. Amalvict M. J. P., Boy and E. Calais. On the use of long records of superconducting and absolute gravity observations with special application to the strasbourg station, france. *Cahiers du Centre Européen de Géodynamique et de Sismologie*, 17:67–83, 2000.
- [31] M. Van Camp. Noise induced by the refrigeration device of a superconducting gravimeter in the seismological station of membach (belgium). *Bulletin d'Informations des Marees Terrestres*, 123:9302–9314, 1995.
- [32] O. Francis, T.M. Niebauer, G. Sasagawa, F. Klopping, and J. Gschwind. Calibration of a superconducting gravimeter by comparison with an absolute gravimeter fg5 in boulder. *Geophysical Research Letters*, 25(11):1075–1078, April 1998.
- [33] T. M. van Dam and O. Francis. Two years of continuous measurements of tidal and nontidal variations of gravity in boulder, colorado. *Geophysical Research Letters*, 25:393–396, 1998.
- [34] H.G. Scherneck. A parametrized solid earth tide model and ocean tide loading effects for global geodetic baseline measurements. *International Journal of Geophysics*, 106:677–694, 1991.
- [35] J. Peterson. Observations and modeling of seismic background noise. *U.S. Dept. of Interior Geological Survey*, 1993.
- [36] M. Van Camp and P. Vauterin. Tsoft manual. 2005.

- [37] M. Van Camp and P. Vauterin. Tsoft: Graphical and interactive software for the analysis of time series and earth tides. *Computers & Geosciences*, 31(5):631–640, 2005.
- [38] F. Roosbeek. RATGP95: a harmonic development of the tide-generating potential using an analytical method. *Geophysical Journal International*, 126:197–204, 1996.
- [39] H.G. Wenzel. The nanogal software: Earth tide data processing package eterna. *Bulletin d'Informations Marees Terrestres*, 124:9425–9439, August 27, 1997.
- [40] H.G. Scherneck. Ocean tide loading provider, July 27th, 2011.
- [41] M.S. Bos and T.F. Baker. An estimate of the errors in gravity ocean tide loading computations. *Journal of Geodesy*, 79:50–63, 2005.
- [42] N.T. Penna, M.S. Bos, T.F. Baker, and H.G. Scherneck. Assessing the accuracy of predicted ocean tide loading displacement values. *Journal of Geodesy*, 82:893–907, 2008.
- [43] J. Arnosó, M. Benavent, and F.G. Montesinos. Updating gravimetric tide parameters and ocean tide loading corrections at the observing sites cueva de los verdes and timanfaya of the geodynamics laboratory of lanzarote. *Instituto de Geociencias*.

